minerals

MDPI

Article

The Submarine Trachytic Lobe–Hyaloclastite Complex of the Caldera of Taburiente (La Palma, Canary Islands): The Age and Meaning of the Oldest Geological Formation on the Island

Ramón Casillas [1,*], Julio de la Nuez [1], Juan Ramón Colmenero [2], Carlos Fernández [3], Fred Jourdan [4], Szabolcs Harangi [5,6] and Réka Lukács [5,6,7]

1 Departamento de Biología Animal, Edafología y Geología, Universidad de La Laguna, P.O. Box 456, 38200 La Laguna, Spain; obelus@telefonica.net
2 Departamento de Geología, Facultad de Ciencias, Universidad de Salamanca, Plaza de la Merced s/n, 37008 Salamanca, Spain; colme@usal.es
3 Departamento de Geodinámica, Estratigrafía y Paleontología, Facultad de Ciencias Geológicas, Universidad Complutense de Madrid, C. de José Antonio Novais, 12, 28040 Madrid, Spain; cafern08@ucm.es
4 Western Australian Argon Isotope Facility, School of Earth and Planetary Sciences, John de Laeter Centre/Space Science and Technology Centre/TIGeR, Curtin University, GPO Box U1987, Perth, WA 6845, Australia; f.jourdan@exchange.curtin.edu.au
5 Department of Petrology and Geochemistry, Institute of Geography and Earth Sciences, Eötvös Loránd University, Pázmány Sétány 1/C, H-1117 Budapest, Hungary; harangi.szabolcs@ttk.elte.hu (S.H.); lukacs.reka@csfk.org (R.L.)
6 MTA–HUN-REN CSFK Lendület "Momentum" PannonianVolcano Research Group, Institute for Geological and Geochemical Research, HUN-REN Research Centre for Astronomy and Earth Sciences, Budaörsi út 45, H-1112 Budapest, Hungary
7 HUN-REN CSFK, MTA Centre of Excellence, Budapest, Konkoly Thege Miklós út 15-17, H-1121 Budapest, Hungary
* Correspondence: rcasilla@ull.edu.es; Tel.: +34-922845268

Abstract

This paper describes for the first time a lobe–hyaloclastite felsic complex on an oceanic island of intraplate setting. In the submarine volcanic succession of the Basal Complex of La Palma (Canary Islands), two main units are identified: an older felsic formation and a conformable upper basaltic–trachybasaltic formation. The felsic formation comprises three facies associations: (1) coherent facies, represented by trachytic lobes with porphyritic, aphanitic, or glass trachytes; (2) autoclastic facies, including hyaloclastites and autobreccias; and (3) syn-eruptive resedimented facies, consisting of mono- and polymictic breccias (massive or graded), and of volcaniclastic sandstones and breccias. The internal architecture and facies relationships are consistent with sedimentation in a submarine trachytic lobe–hyaloclastite complex, which predates the basaltic–trachybasaltic formation. These felsic rocks are classified as trachytes, although they exhibit extensive hydrothermal alteration. The behavior of incompatible trace elements suggests that the variety of the trachytic rocks—porphyritic or aphanitic terms—can be attributed to fractional crystallization processes. However, the features of the incompatible trace elements and the rare earth elements indicate that these trachytes are not cogenetic with the submarine basaltic–trachybasaltic rocks of the Basal Complex of La Palma. Instead, the trachytic magmas responsible for the lobe–hyaloclastite complex formation likely represent the late evolution of a precursor basaltic magma that would have led to the formation of a basaltic submarine shield not exposed nowadays. This study also presents the first robust geochronological constraints for the submarine volcanic units of the La Palma Basal Complex, based on U–Pb on zircons and Ar–Ar on amphiboles. Given that the submarine trachytic lobe–hyaloclastite complex is the oldest lithostratigraphic unit exposed on La Palma, a minimum age of 3.10 Ma is proposed for the initiation of the island submarine growth stage.

check for updates

Academic Editors: Enrique Merino Martínez and Helena Sant'Ovaia

Received: 12 July 2025
Revised: 9 September 2025
Accepted: 16 September 2025
Published: 23 September 2025

Citation: Casillas, R.; de la Nuez, J.; Colmenero, J.R.; Fernández, C.; Jourdan, F.; Harangi, S.; Lukács, R. The Submarine Trachytic Lobe–Hyaloclastite Complex of the Caldera of Taburiente (La Palma, Canary Islands): The Age and Meaning of the Oldest Geological Formation on the Island. *Minerals* **2025**, *15*, 1007. https://doi.org/10.3390/min15101007

Keywords: Caldera de Taburiente; La Palma; lobe–hyaloclastite complex; trachytes

1. Introduction

The origin and evolution of magmatism associated with the source and growth of oceanic islands in an intraplate setting is currently one of the topics that causes the most discussions and debates within the scientific community related to the study of the genesis and evolution of magmas on Earth. Central to this debate are the mechanisms of magma genesis and evolution, not only the possible interactions between the mantle and the oceanic crust, but also the respective roles of the asthenosphere and the lithosphere [1–10].

The Canary Islands have played a prominent role in this scientific discussion. Since the 1970s, numerous hypotheses have been proposed to explain the origin and evolution of magmatism in the archipelago. Some of these models invoke a passive role of the oceanic lithosphere, such as the hotspot hypothesis [1,2], the "blob" hypothesis [3], the edge-driven convection [4], and the combined hotspot–edge convection hypothesis [5,6]. Alternatively, active tectonic models have also been proposed, including the propagating fracture model [7], the uplifted block hypothesis [8], the synthetic model [9], and the plate-based hypothesis [10]. The diversity of these hypotheses reflects the Canary Islands' unique geological setting, which offers an unbeatable setting to study lithosphere–asthenosphere interactions in intraplate volcanic environments.

Unfortunately, most of these models have predominantly focused on the subaerial evolution of the island volcanic edifices, while the earlier submarine growth stage has received comparatively limited attention. This imbalance likely stems from the scarcity of robust geochronological data for the early submarine units, chiefly the Basal Complexes of the islands, and the inherent difficulties involved in their investigation.

On the other hand, in recent years, increasing attention has been directed toward understanding the submarine construction of oceanic islands and volcanic seamounts. Seamounts (including "guyots") are volcanic structures that rise from the ocean floor, either along mid-ocean ridges ("on-ridge") or on older oceanic crust ("off-the-axis") [11]. Global inventories vary: refs. [12,13] catalogued 24,643 seamounts (8458 of which exceed 1 km in height), while ref. [14] identified 10,234 "seamounts" and "guyots" higher than 1 km. Other estimates include 11,880 [15], 14,287 [16], and 33,452 [17] seamounts.

Much of the information about the distribution, morphology, size, structure, and growth of submarine volcanoes has been acquired using surface and immersion analytical techniques. These include bathymetric mapping [18–47]; dredging and drilling of seamounts, volcanic-island aprons, and ocean floor materials [29–32,41,48–71]; deep drilling on oceanic islands (e.g., Hawaii [51,72,73]; Canary Islands [74]); visual observations using submersible vehicles [36–38,40,46,75–88]; sampling using submersible vehicles [36,40,54,62,79–83,87–92]; permanent sensor networks [93–97]; geophysical studies of internal structures [30,31,35,45,46,60,91,98–105]; and surface studies of subglacial or emergent seamounts [50,106–124].

Focusing on the emergent seamount of La Palma, ref. [108] proposed a three-stage model for the submarine evolution of a seamount in an intraplate setting [122]:

(a) Small seamount stage (100–1000 m in height).
(b) Medium seamount stage (height > 1000 m; eruptive depth > 700 m).
(c) Explosive seamount stage (eruptive depth < 700 m).

In the Canary Islands—specifically on La Palma, La Gomera, and Fuerteventura—the submarine growth is primarily represented by rocks of their respective Basal Complexes [108,123–125], although these complexes also include remnants of the oceanic crust,

plutonic rocks, and dyke complexes related to the growth of the earliest submarine and subaerial edifices, and a varied set of breccia materials [108,109,115–117,124–175].

Consequently, in certain islands such as La Palma, the conditions are uniquely favorable for studying the submarine growth and emergence of an oceanic island through direct field observation of exposed units.

Geological Background

La Palma is the northwesternmost island of the Canary Archipelago. The island rises up to 2426 m above sea level (Roque de los Muchachos), from an abyssal plain located at a depth of about 4000 m [176], although during earlier geological stages, this level was exceeded [162]. La Palma also exhibits the steepest average slope among the Canary Islands. The oceanic lithosphere beneath the island records the M25 magnetic anomaly, Jurassic age [177].

From a geological, geographical, and geophysical standpoint (Figure 1), La Palma can be divided into two morphostructurally distinct regions. The northern part of the island has a well-defined hexagonal perimeter and a roughly conical morphology, with the impressive Caldera de Taburiente located near its center. This prominent feature drains southwestward via the Barranco de Las Angustias, whereas along its perimeter, it displays numerous deep ravines, radiating outwards toward the sea.

In contrast, the southern region of La Palma is defined by a "gabled roof"-shaped topography with relatively few ravines. This zone trends N–S and forms the Cumbre Vieja volcanic ridge.

The northern part represents the oldest part of the island, composed of a denser, more rigid insular core [178–180]—referred to as the North Shield—which is inferred to root into the upper mantle. The oldest exposed rocks of this shield occur within the Caldera de Taburiente and in the Barranco de las Angustias. These include uplifted submarine units, such as trachytic breccias and lava flows, along with the trachybasaltic and basaltic breccias and the pillow lavas of the Barranco de Las Angustias [108,109,128,129,136,154,173,174,181].

These submarine units, representing part of the submarine growth stage of the North Shield, are uplifted and tilted, with bedding dipping up to 70° to the SW, and exhibit a low-grade (greenschist facies) hydrothermal metamorphism. This has led to the recrystallization of the primary minerals of the gabbros into green-colored species, such as albite, chlorite, epidote, actinolite, prehnite, andradite, and others [129,182,183]. These mineral assemblages suggest peak metamorphic conditions of 450–490 °C and 1–1.5 kbar. Therefore, it is estimated that ~3000 m of overburden once covered these submarine rocks, whose top is now exposed at ~1300 m a.s.l. inside the Caldera de Taburiente.

These submarine rocks contain microfossil assemblages of the Lower Pliocene age [109,184] and are intruded by pyroxenites, gabbros, olivine gabbros, amphibolic, alkaline gabbros, and syenites, and a dense network of basaltic sheeted dykes [108,136,162,173].

The subaerial growth stage of the North Shield [185–193] commenced with the formation of the Garafía Volcano (Figure 1, 1.72–1.2 Ma), now only partially exposed through erosional windows at the headwaters or in the middle course of the deepest ravines in the north, such as the Barranco del Agua, Gallegos, Franceses, de los Hombres, and Jieque ravines, amongst others [185,190,194]. This edifice consists predominantly of pyroclastic and basaltic flows. The lavas occur tilted periclinally ~30°, suggesting that the Garafía Volcano developed as a large shield, whose center almost coincided with the Caldera de Taburiente [195]. The estimated thickness of this unit is ~400 m, with a summit around 2000 above sea level. The Garafía Complex is crossed by numerous dykes, especially toward its central region.

The Garafía Volcano suffered a lateral landslide—the Santa Cruz de La Palma landslide—on its southeastern flank, generating important debris–avalanche deposits now exposed within the Caldera de Taburiente [154,186,196–201].

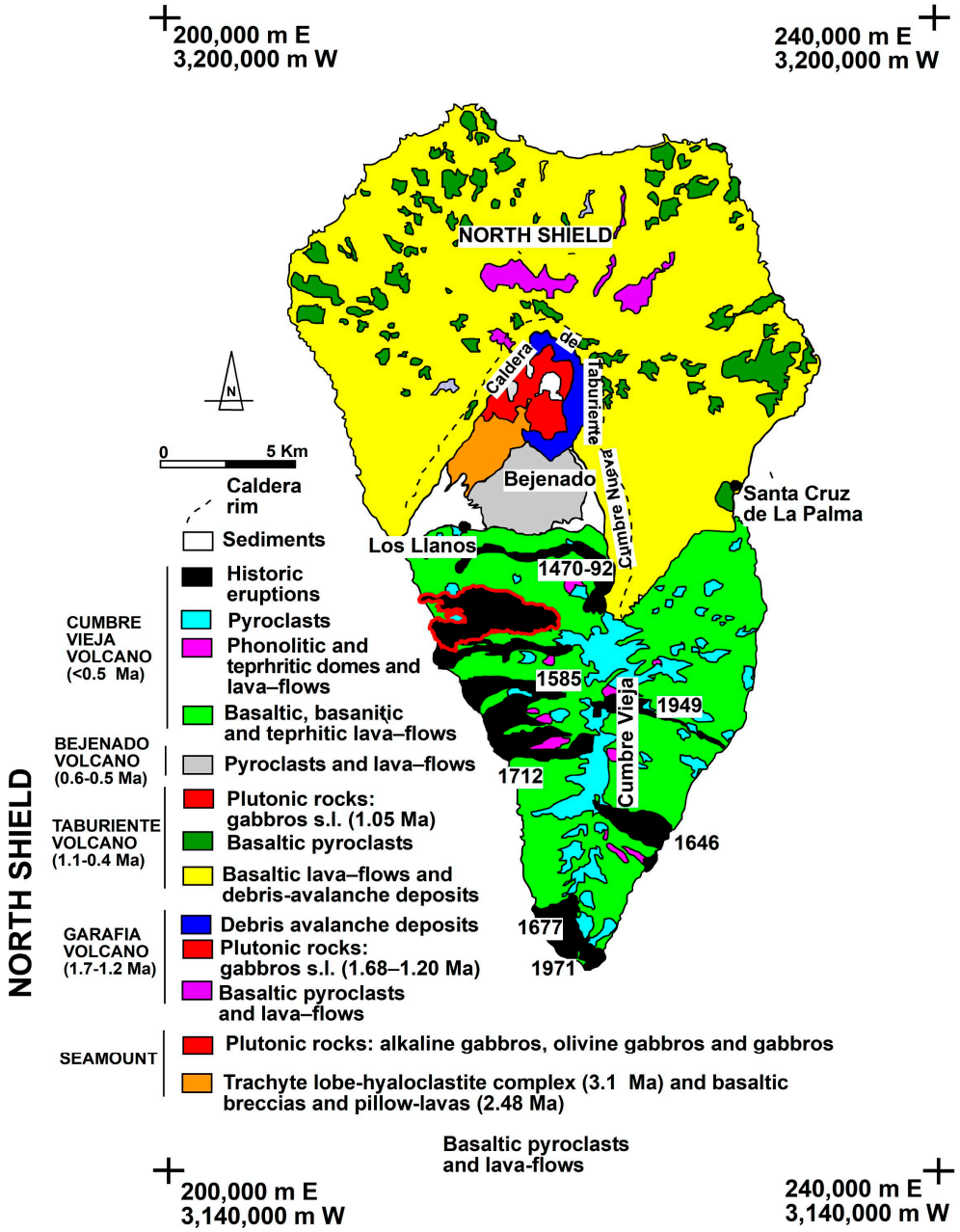

Figure 1. A geological map of La Palma Island (modified from [201,202]). The historical eruption outlined in red is the one from 2021. Coordinates in U.T.M. Hayford ellipsoid projection.

Subsequently, the Taburiente Volcano developed on the remains of the Garafía Volcano, nested in the amphitheater created by the Santa Cruz de La Palma landslide (Figure 1). This edifice is subdivided into a Lower Taburiente Unit (1.08–0.83 Ma) and an Upper Taburiente Unit (0.77–0.44 Ma), both dominated by basaltic lava flows and pyroclastic deposits. The volcano experienced a major gravitational collapse on its SW flank: the Playa de la Veta landslide (~0.83 Ma, [201,202]). Following this event, a reorganization of the eruptive centers took place, and from being localized in the center of the shield, it became increasingly concentrated into three rift zones (NW, NE, and N–S), converging near the shield's geometric center [154]. Continued accumulation, more than 500 m thick, led to a

large edifice reaching ~3000 m above sea level, composed predominantly of pyroclastic and mostly basaltic lavas, and some terminal episodes of a tephritic and phonolitic nature [154].

The greatest eruptive activity became progressively concentrated in the N-S rift (Cumbre Nueva ridge), which became increasingly higher and more unstable, and ultimately collapsed, generating a large landslide on the western flank of the edifice, the Cumbre Nueva landslide [186,188,194]. The resulting large depression was subsequently infilled with younger lava flows and ultimately evolved into the present Caldera de Taburiente. The slide has been dated at 0.56 Ma, which is the age of the topographically highest lavas at Cumbre Nueva affected by the collapse [190].

Inside the Caldera de Taburiente, a series of plutonic bodies and dyke swarms of diverse compositions intrude into the submarine formations and some of the debris–avalanche deposits related to the Santa Cruz de la Palma landslide. These plutons are formed by alkaline gabbros, olivine gabbros, gabbros, and some syenites dated at 1.68–1.05 Ma [181] and are interpreted as the magmatic chambers that fed the Garafía and Taburiente edifices [136,181,195].

The submarine volcanic rocks and the oldest parts of the later subaerial volcanic edifices (Garafía and Taburiente Volcanoes) were affected by at least three stress fields, which strongly influenced the geometry and succession of the vein injection and plutonic intrusion systems. These stress fields were caused by the interaction of local stress sources related to the large volcanic edifices and regional fields caused by the state of stress on the African plate in the sector [195]. According to [195], four distinct dyke systems exist. The first two systems, I and II, coincide with the dyke systems 1 (with highly variable orientation) and 2 (sills with NW-SE directions, inclined about 53° to the SW) of [109] and are related to the submarine growth of the island. The third system, III-1, has essentially a radial arrangement and is related to the formation of the Garafía Volcano. The fourth system, III-2, also radial, is linked to the growth of the Taburiente Volcano.

Regarding the stress field tensors, stress field 1 post-dates dyke systems I and II, field 2 was contemporary with the dyke system III-1, and field 3 was contemporary with the dyke system III-2. Stress fields 1 and 2 were active between 1.7 and 1.2 Ma, while stress field 3 would have affected the island after 1.08 Ma.

Inside the amphitheater left by the Cumbre Nueva landslide, a new volcano, the Bejenado Stratovolcano, was formed (Figure 1, ~0.56–0.49 Ma), ending the North Shield growth. The Bejenado activity started with basaltic flows and pyroclasts, while its final phase was made up of basaltic, basanitic, tephritic, and phonolitic pyroclastic and lavas, which represent the most differentiated phase of the North Shield and form the 600 m thick volcanic rocks of the Bejenado volcano [154].

The Cumbre Vieja Volcano is likely younger than 0.4 Ma [154,192] and forms a 15 km long N–S trending active volcanic ridge that has undergone several historic eruptions over the last 500 years. It is composed of stacked lava flows and pyroclasts from numerous fissure eruptions, with emission centers preferentially concentrated along the N–S line of summits and lavas spilling out on both flanks of the ridge. Older basaltic and basanitic eruptions (~150 ka and older [192]) formed the western cliff, while basaltic, basanitic, and tephritic strombolian eruptions and more recent phonolitic lava domes formed the entire Cumbre Vieja cover and extensive coastal lava platforms, with ages ranging from 50 Ka to the present [154,187,188,202,203]. This volcano has been one of the most active of the Canary Islands in historical times, since, in addition to the subhistoric eruption of Montaña Quemada (which occurred between 1470 and 1492), there have been six other eruptions: Tahuya (1585), Tigalate or Martín (1646), San Antonio (1677), El Charco (1712), San Juan (1949), Teneguía (1971), and Hoya de las Plantas (2021) [204–207] (see Figure 1). These eruptions have all been fissural, with effusive strombolian activity, sporadically, phreatomagmatic, emitting fundamentally basanitic, and in some cases, tephritic, lavas.

Some of these eruptions developed lava flows that reached the coastline, forming important lava deltas (Figure 1).

As previously discussed, the submarine stage of La Palma includes a felsic episode and a subsequent basaltic–trachybasaltic episode [129]. Both are intruded by gabbroic bodies that caused intense contact metamorphism and by a complex network of basaltic dykes associated with both the submarine and subaerial phases [136]. The intense heating caused by these intrusions, together with the circulation of meteoric waters within the volcanic edifice, caused intense hydrothermal metamorphism that especially affected the felsic rocks. As a result, while the basaltic–trachybasaltic episode has been well characterized and dated as Pliocene [108], the felsic unit, which is also poorly exposed, has hardly been studied in depth and only interpreted in a general way as intrusive trachytic- or phonolitic-flow domes within the basaltic–trachybasaltic succession [154].

This work presents a preliminary genetic study of the felsic episode, including detailed field mapping, stratigraphic logging, facies analysis, geochemical characterization, and age determinations.

2. Materials and Methods: Spectroscopy

Major and trace element analyses of whole-rock samples were conducted at Activation Laboratories Ltd. (Ancaster, ON, Canada). Major elements (Si, Al, Ti, Mg, Fe, Mn, Ca, Na, K, and P) and some trace elements (Sr, Y, Zr, Ba, and V) were measured using Fused Bead Inductively Coupled Plasma (FUS-ICP) on lithium metaborate/tetraborate fused glass disks. Most other trace elements (Cu, Co, Ni, Zn, Ga, Rb, Nb, Hf, Ta, Pb, Th, U, and REEs) were analyzed via Inductively Coupled Plasma Mass Spectrometry (ICP-MS). Chromium (Cr) and scandium (Sc) concentrations were determined by Instrumental Neutron Activation Analysis (INAA). Volatile content was assessed via Loss on Ignition (LOI) at 1000 °C. The complete analytical results are provided in Table S1.

Four trachyte samples (TAB-12, TAB-23, TAB-24, and TAB-33B) from lobes of the submarine lobe–hyaloclastite complex and one trachybasalt pillow-lava sample (TB-28B) were collected at different stratigraphic levels along the stratigraphic section of the Barranco de las Angustias.

Mineral separation to obtain zircon and amphibole crystal concentrates was carried out on these samples at the Mineral Separation Laboratory of the Department of Petrology and Geochemistry at Eötvös Loránd University in Budapest, Hungary. The separations yielded zircon crystals from the four trachyte samples and amphibole crystals from the only trachybasalt pillow-lava sample.

Isotopic determinations using the U-Pb method on the zircon concentrates (20 measurements per sample) were performed using a SHRIMP II/mc ion microprobe at the IBERSIMS Laboratory Service of the Scientific Instrumentation Center of the University of Granada. Hand-picked zircons from the studied samples, several grains of the TEMORA-1 standard (for isotope ratios; [208]), one grain of the SL13 zircon standard (for U concentration, [209]), plus a few grains of the REG zircon (with high common Pb content, for mass calibration) were cast in a 3.5 cm diameter epoxy mount (megamount), polished, and imaged using optical (reflected and transmitted light) and scanning electron microscopy (SEM), including secondary electrons (SEs) and cathodoluminescence (CL). After extensive cleaning, the mounts were coated with ultra-pure gold (8–10 nanometers thick) and analyzed under the SHRIMP. Analytical procedures followed [210]. Each selected spot was rastered for 120 s with the primary beam before measurement and then subjected to 6 scans, following the isotope peak sequence $^{196}Zr_2O$, ^{204}Pb, $^{204.1}$background, ^{206}Pb, ^{207}Pb, ^{208}Pb, ^{238}U, ^{248}ThO, and ^{254}UO.

Each peak was measured 10 times per scan, with counting times of 2 s (mass 196), 5 s (masses 238, 248, and 254), 15 s (masses 204, 206, and 208), and 20 s (mass 207). The primary beam ($^{16}O^{16}O$-) was ~5 nA, with a 120 µm Köhler aperture, producing 17 × 20 µm elliptical spots. The secondary ion beam slit was 80 µm, achieving ~5000 resolution at 1% peak height.

Calibration was performed using standards on the same mount. The REG zircon (ca. 2.5 Ga, very high U, Th, and common lead content) was used for mass calibration, SL13 (238 ppm U) for U concentration, and TEMORA-1 (416.8 ± 1.1 Ma) for isotope ratios. TEMORA-1 was analyzed every four unknowns to monitor analytical consistency.

Data reduction was conducted using SHRIMPTOOLS software (2014), developed by F. Bea for IBERSIMS (accessed on 20 January 2025), based on the 2.4.0 PRAWN software (2020) and compatible with Ludwig's SQUID. SHRIMPTOOLS is platform-independent and runs on Windows, Mac, or Unix computers independently of the language, time, and date system settings. It has been written in the programming language of the STATA commercial package, which implements powerful algorithms for robust regression, outlier detection, and time-series analysis. Isotope intensities were calculated by averaging replicate measurements (excluding outliers), correcting for background (204.1 mass), and normalizing to standard beam monitor (SBM) values. Isotopic ratios (204/206, 207/206, 208/206, and 254/238) were computed using Dodson's [211] double-linear interpolation method. Ratios involving 206/238, 206/195, 238/195, and 248/254 were calculated by dividing the value at the mid-time of the analysis of each isotope, calculated from the robust regression lines of the peak average of each scan vs. the time at which it was measured. Errors for Dodson interpolated ratios were calculated as the standard error of the (scans-1) interpolations for each ratio. Errors for the isotope ratios were calculated by the regression results from propagating the standard error of the linear prediction at the mid-point of the analysis. $^{206}Pb/^{238}U$ was calculated from the measured $^{206}Pb+/^{238}U+$ and UO+/U+, following the method described by [212]. The error reported for $^{206}Pb/^{238}U$ includes (1) the error in UO+/U+; (2) the error in the regression line ln(UO+/U+) vs. ln ($^{206}Pb/^{238}U$); (3) the standard error in the replicate measurements of the TEMORA zircon. For high-U zircons (U > 2500 ppm), $^{206}Pb/^{238}U$ is further corrected using the algorithm of [213]. Though seldom necessary, the software also permits correction for instrumental drift with time using the sequence of replicate measurements of the TEMORA zircon.

Negative ^{204}Pb values may result from the subtraction of the blank signal from the measured ^{204}Pb peak when the latter is extremely low—typically zero, one, or two counts per 10 s. For instance, if no counts are recorded at mass 204 and a single count is recorded at 204.06 (the blank), the resulting $^{204}Pb/^{206}Pb$ ratio becomes negative. Although such negative isotope ratios lack physical meaning, there is consensus within the SHRIMP user community that these values should be retained for two primary reasons: (1) to maintain balanced averaging across multiple measurements and (2) to mitigate the effects of anomalously high blank values. Since blank corrections are also applied to masses ^{207}Pb and ^{206}Pb, preserving negative ^{204}Pb values can help achieve more accurate $^{207}Pb/^{206}Pb$ ratios. In this study, negative ^{204}Pb values were retained in accordance with standard practice, as they are statistically valid and contribute to the reliability of isotopic ratio corrections.

The analytical results are provided in Table S2. The images of zircon grains by cathodoluminescence, in transmitted and reflected light, including the analyzed spots (in the cathodoluminescence images), are shown in Figure S1. In general, for samples such as this one, the preferred age is the $^{06}Pb/^{238}U$ age corrected for common Pb (207-corrected), which generally coincides with the intersection age.

$^{40}Ar/^{39}Ar$ analyses were performed at the Western Australian Argon Isotope Facility, Curtin University. Samples were step-heated using a 110 W Spectron Laser System equipped with a continuous Nd:YAG laser (IR; 1064 nm) and rastered over the sample for one minute to ensure a homogenously distributed temperature. The gas was purified through a stainless-steel extraction line using two SAES AP10 getters, a GP50 getter, and a liquid nitrogen condensation trap. Argon isotopes were measured in static mode using an MAP 215–50 mass spectrometer (resolution ~500; sensitivity 4×10^{-14} mol/V) with a Balzers SEV 217 electron multiplier. Each sample was run in 9–10 peak-hopping cycles. Data acquisition was managed with the Argus program (M.O. McWilliams) in the LabVIEW environment. Data reduction was performed using ArArCALC software [214], with decay constants from [215]. Blanks were monitored every 3–4 steps, with typical ^{40}Ar blanks ranging from 1×10^{-16} to 2×10^{-16} mol. Argon isotopic data were corrected for blanks, mass discrimination, and radioactive decay and, along with the age, K/Ca values, and inverse isochron plots, are presented in Table S3, with individual uncertainties reported at the 1σ level.

Plateaus were defined by the following criteria: (i) plateaus must include at least 70% of ^{39}Ar released; and (ii) they should be distributed over a minimum of 3 consecutive steps agreeing at the 95% confidence level and satisfying a probability of fit (P) of at least 0.05. Plateau ages were reported at the 2σ confidence level, calculated as the weighted mean of plateau steps based on the inverse variance of their individual analytical error. Inverse isochrons include all steps with $p \geq 0.05$. All uncertainties (in square brackets) were estimated using the Monte Carlo approach of [216].

3. Results and Discussion

3.1. Description and Interpretation of Facies

The trachytic episode (Figure 2) forms a stratigraphic unit that crops out with a NW-SE trend, dipping to the SW between 15° and 62°. Its base is located towards the center of the Caldera, whereas its top, in stratigraphic continuity with the overlying upper submarine trachybasaltic–basaltic sequence, is visible in the Barranco de Las Angustias, near El Carbón. The relative position of both units and their stratigraphic continuity show that the trachytic episode is not intrusive into, but actually older than, the intermediate–basic series and hence constitutes the oldest formation cropping out on the island of La Palma. The stratigraphy of the submarine trachytic episode has been studied along the Barrancos de Taburiente and Las Angustias, from about 500 m south of the camping area of the National Park in the Barranco de Taburiente to El Carbón (points A and B, respectively, in Figure 2). The resulting stratigraphic log, about 330 m thick (Figure 3), characterizes this unit from the deepest and most internal levels to the shallowest and most distal part of the submarine trachytic episode. Three main facies, with several subfacies, have been recognized (Table 1):

(a) Coherent facies (Table 1A).
(b) Autoclastic facies (Table 1B).
(c) Resedimented syn-eruptive facies (Table 1C).

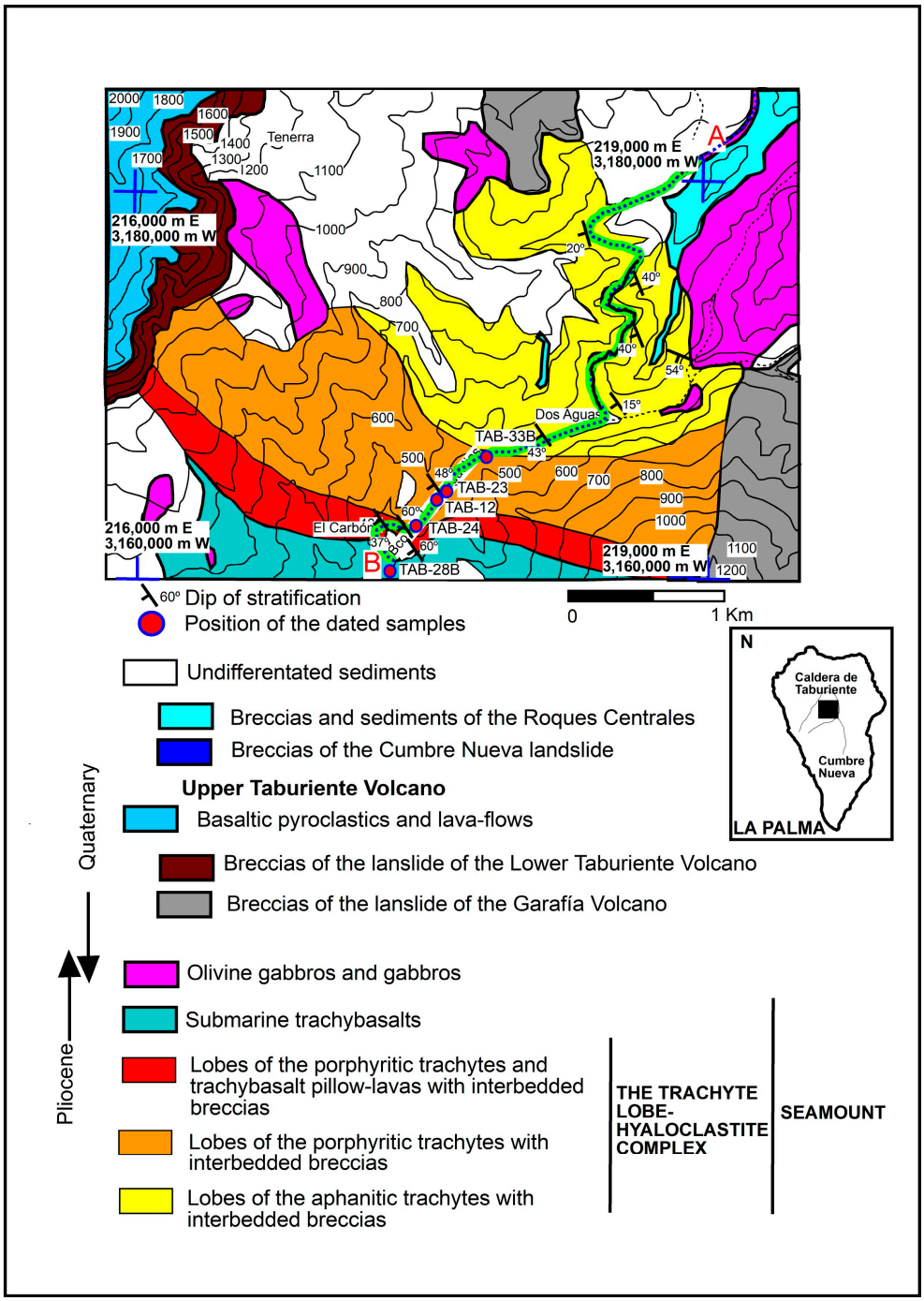

Figure 2. A geological map of the central sector of the Caldera de Taburiente. The inset indicates the location of the mapped area within La Palma Island. The green solid line marks the stratigraphic section studied from point A to point B through the Barranco de Taburiente and the Barranco de las Angustias. The geological units mapped may not directly correspond to the lithofacies described in Table 1A–C. Coordinate system: UTM, Hayford ellipsoid projection.

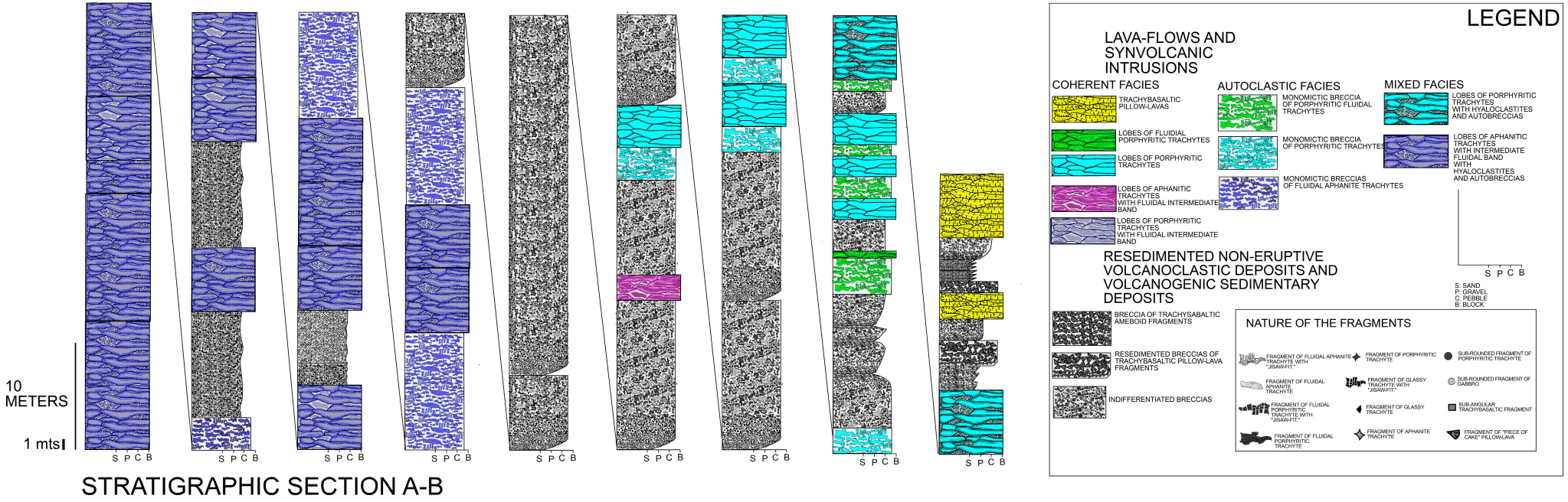

Figure 3. A stratigraphic log of the studied interval measured along the Barranco de Taburiente and the Barranco de Las Angustias (A–B section in Figure 2). The characteristics of the different facies and subfacies are described in Table 1.

Table 1. (**A**) Description and interpretation of the coherent facies from the trachytic episode of the Caldera de Taburiente. (**B**) Description and interpretation of the autoclastic facies from the trachytic episode of the Caldera de Taburiente. (**C**) Description and interpretation of the resedimented syn-eruptive facies from the trachytic episode of the Caldera de Taburiente.

	Facies	Litology, Stratification, Textures, and Structures	Interpretation
		A	
A: COHERENT FACIES	A1. TRACHYBASALTIC PILLOW LAVAS	Very vesiculated pillow lavas forming continuous tubes up to 1 m in diameter (Figure 4-1). Little hyaloclastic material occurs among the pillow lavas.	*Lava flows* from submarine trachybasaltic eruptions.
	A2. LOBES OF VITREOUS OR APHANITE TRACHYTES	Aphanitic or vitreous trachytes in tubular bodies, in the form of lobes, with individual diameters varying between 0.5 and 1 m, superimposed until reaching thicknesses of up to 20 m. In the lobes (Figure 4-2), a zoning from core to edge is observed: (1) Core: Aphanitic or vitreous trachyte, black or gray-violet in color, with a vitreous micro-cryptocrystalline, fluidal, feldspathic, spherulitic, and carbonate matrix (Figure 4-2B). (2) Internal intermediate zone of aphanitic or glassy trachyte, in most cases with flow banding (Figure 4-2B). (3) External intermediate zone of white aphanitic trachyte with vesicles (5%–20%) of green color (with calcite, albite, and epidote) and stretched up to 2 cm long (Figure 4-2B). (4) External edge of vitreous trachyte about 2–3 cm thick and greenish or black in color (obsidian transformed to chlorite), (Figure 4-2B).	*Trachytic lobes* (similar to those described by [217–219]. Here, they are described on oceanic islands for the first time.
	A3. LOBES OF PORPHYRITIC TRACHYTES	Light or gray porphyritic trachytes in tubular bodies, in the form of lobes, with individual diameters varying between 0.5 and 1 m, superimposed until reaching thicknesses of up to 30 m (Figure 4-3). Lobes may have no internal zoning with (subfacies A.3.1.) or without fluid texture (subfacies A.3.2.) or show a core-to-edge zonation (subfacies A.3.3.) (Figure 4-3C): (1) Porphyritic trachyte core, with phenocrysts of plagioclase, potassium feldspar (up to 3–4 cm, altered to albite and epidote), biotite (up to 2 mm, altered to chlorite, epidote, and opaque minerals), opaques, and apatite. Microcrystalline, feldspathic, non-fluidal, spherulitic matrix, with some epidote, opaques, and chlorite. They barely present varioles. (2) Internal intermediate zone of porphyritic trachyte with frequent flow banding. (3) External intermediate zone of white porphyritic trachyte with stretched green vesicles (5%–20%) (with calcite, albite, and epidote) up to 2 cm long. (4) External edge (2–3 cm thick) of greenish or black vitreous trachyte (obsidian transformed to chlorite), with some scattered feldspar microliths.	*Trachytic lobes* (similar to those described by [217–219]. Here, they are described on oceanic islands for the first time.

Table 1. *Cont.*

	Facies	Litology, Stratification, Textures, and Structures	Interpretation
		B	
B: AUTOCLASTIC FACIES	B1: HYALOCLASTITES	Clast-to-matrix-supported monomictic breccia, poorly sorted, ungraded, with little matrix, arranged in massive layers less than 10 m thick with gradational contacts with adjacent trachytic bodies (Figure 4-4). Clasts up to 30 cm in size (2–3 cm on average), angular and subangular with polyhedral or "blocky" shapes, curviplanar margins, straight corners and, more rarely, with amoeboid shapes. Some exhibit "jigsaw-fit" or clast-rotated textures with gradual transit from the lobes to the breccias with jigsaw-fit textures and from these to the breccias with clasto-rotated textures. The nature of the clasts is the same as that of the adjacent trachytic lobes: porphyritic trachytes (subfacies B.1.1.), fluidal porphyritic trachytes (subfacies B.1.2.), or fluidal aphanitic trachytes (subfacies B.1.3.), with varied vesiculation (stretched or rounded vesicles).	*"In situ" hyaloclastites, generated by fragmentation and contraction of the trachytic lobes* due to rapid cooling in contact with sea water [220–222]. In submarine conditions, the contact of water with magma or with rock that is still hot produces non-explosive fragmentation due to supercooling and contraction, generating hyaloclastites. If the magma was in the process of degassing, the hyaloclastites appear with a high degree of vesiculation, giving rise to pumice-like clasts.
	B2: AUTOBRECCIAS	Clast-supported monomictic breccia, poorly classified, massive and with little matrix, forming layers less than 3 m thick, although they can reach 10 m. Gradational contact with the trachytic lobes (Figure 4-5). Clasts between 3 cm and 50 cm, amoeboid in shape, or, more rarely, angular, and frequently plastically deformed. They present "jigsaw-fit" and clast-rotated textures. The nature of the clasts is the same as that of the adjacent trachytic lobes: porphyritic trachytes (subfacies B.2.1.), fluidal porphyritic trachytes (subfacies B.2.2.), or fluidal aphanitic trachytes (subfacies B.2.3.), with varied degrees of vesiculation (vesicles are stretched or rounded).	*Auto-brecciation or fracturing of the edges of the trachytic lobes* due to the shear or tensional stress that is generated between the moving magma and the edge of the already solidified lobe [218]. If fragmentation occurs under plastic conditions, the clasts are very irregular and adapt to each other [220]. If it is more brittle, clast accumulations with curviplanar surfaces occur [221].
		C	
C: RESEDIMENTED SYN-ERUPTIVE FACIES	C1: TRACHYTIC BRECCIAS, MASSIVE OR WITH SLIGHT NORMAL GRADING	Monomictic, clast-to-matrix-supported breccia, poorly sorted, massive or with slight normal grading, in layers up to 3 m thick (Figure 4-6A,B). Angular to subangular clasts, with an average diameter of 1.5 cm and maximum 20 cm, with polyhedral and, more rarely, amoeboid morphologies, of porphyritic trachytes and aphanitic, fluidal or not, and with varying degrees of vesiculation.	*Submarine mass flows (debris flows)* produced by the resedimentation of hyaloclastites and autobreccias [222].
	C2: POLYMICTIC MASSIVE BRECCIAS	Polymictic clast- and matrix-supported breccia, massive and very poorly classified, with clasts with diameters between 0.5 cm and 2 m (average 5 cm) (Figure 4-6C,D). The clasts are of a very varied nature: subangular with porphyritic trachytes; white trachytes with stretched vesicles; gray aphanitic trachytes and fluidal trachytes (of sizes greater than 2 m that appear to represent large fragments of trachytic lobes); and subangular clasts of trachybasalts and subrounded clasts of gabbros and monzonites.	*Submarine mass flows (debris flows)* produced by small avalanches of hyaloclastites, autobreccias, and lobes of the lobe–hyaloclastic complex and of the pillow lavas and breccias of fragments of trachybasaltic pillows. Clasts larger than 2 m appear to represent large fragments of the trachytic lobes. Subrounded clasts of gabbros and monzonites indicate abrasion during or prior to transportation. The subrounded plutonic rock pebbles could be enclaves transported by felsic magma torn from deep within an already solidified magma chamber, or come from a nearby emerged and exhumed volcanic edifices.

Table 1. *Cont.*

	Facies	Litology, Stratification, Textures, and Structures	Interpretation
C: RESEDIMENTED SYN-ERUPTIVE FACIES	C3: POLYMICTIC MASSIVE BRECCIAS WITH INVERSE GRADATION AT THE BASE	Mono- and polymictic clast- and matrix-supported breccia, medium to poorly sorted, of subrounded and subangular clasts with a minimum size of 2 cm and a maximum of 30 cm (average of 10 cm). Sand and gravel size matrix. The layers show inverse grading at the base and, in some cases, normal grading at the top. The clasts are porphyritic trachytes with a glassy or microcrystalline matrix and stretched vesicles; fluid porphyritic trachytes; aphanitic trachytes, vitreous, more or less fluid; porphyritic trachybasalts, very vesiculated, with curviplanar shapes ("pie pieces") and curved cooling or amoeboid edges, and rounded edges of gabbros and monzonites. We distinguish the following subfacies: subfacies C.3.1. (Figure 4-7), if the clasts are exclusively porphyritic trachybasalts, very vesiculated, with curviplanar shapes ("pie pieces") and curved or amoeboid edges; subfacies C.3.2. (Figure 4-8), if the clasts are exclusively trachytes; subfacies C.3.3. (Figure 4-9), if clasts of trachytes, trachybasalts, and gabbros, and monzonites exist.	*Submarine gravity flows* from the resedimentation of lobes, slipped pillow lavas, hyaloclastites, and autobreccias of trachytic or trachybasaltic composition. These subaqueous gravity flows would be "high-density gravelly turbidity currents" in the sense of [220]; or concentrated density flows of [223]) composed predominantly by grain size populations 2 and 3 of [224] or A and B by [225]. The observed facies would correspond to the R2 parts of a high-density turbidite defined by [220] or to the F2 deposits of an idealized turbidite by [225]. The subrounded clasts of plutonic rocks could have the same origin, as indicated for facies C2.
	C4: POLYMICTIC SANDSTONES AND BRECCIAS WITH INVERSE GRADING AT THE BASE	Coarse sandstones and breccias arranged in stacked inversely graded units 1 to 3 m thick, with subangular clasts of trachybasalts and porphyritic trachytes up to 20 cm in the upper part of each unit (Figure 4-10). The trachytes are highly vesiculated, reaching, in some cases, 40% vesiculation.	*Submarine gravity flows* possibly of turbidite currents: S2 of [224] resulting from transformation of the high-density gravel turbidite currents that formed the massive polymictic breccias with inverse grading at the base (C3).

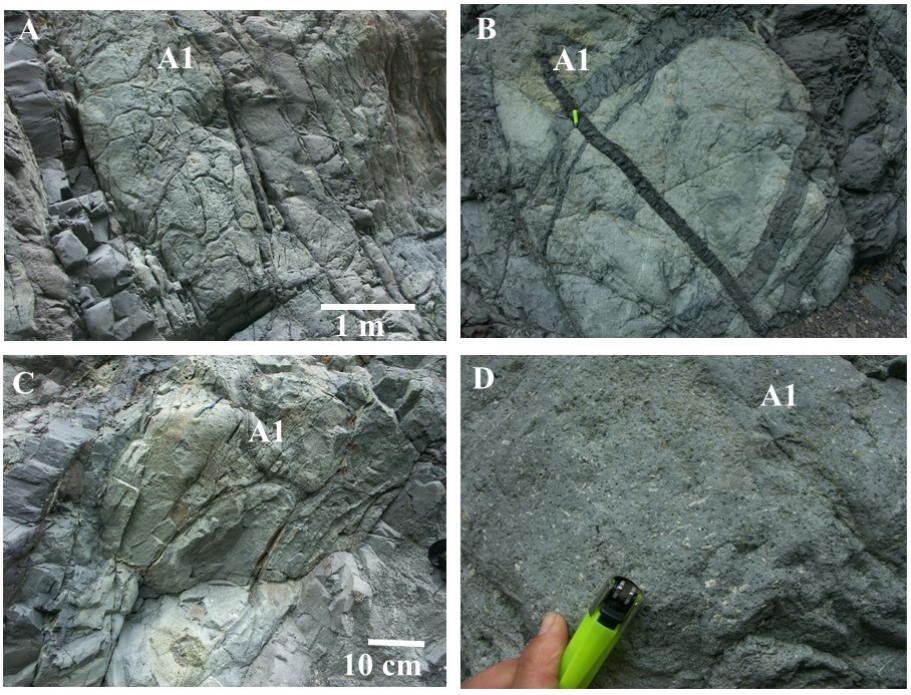

(**1**)

Figure 4. *Cont.*

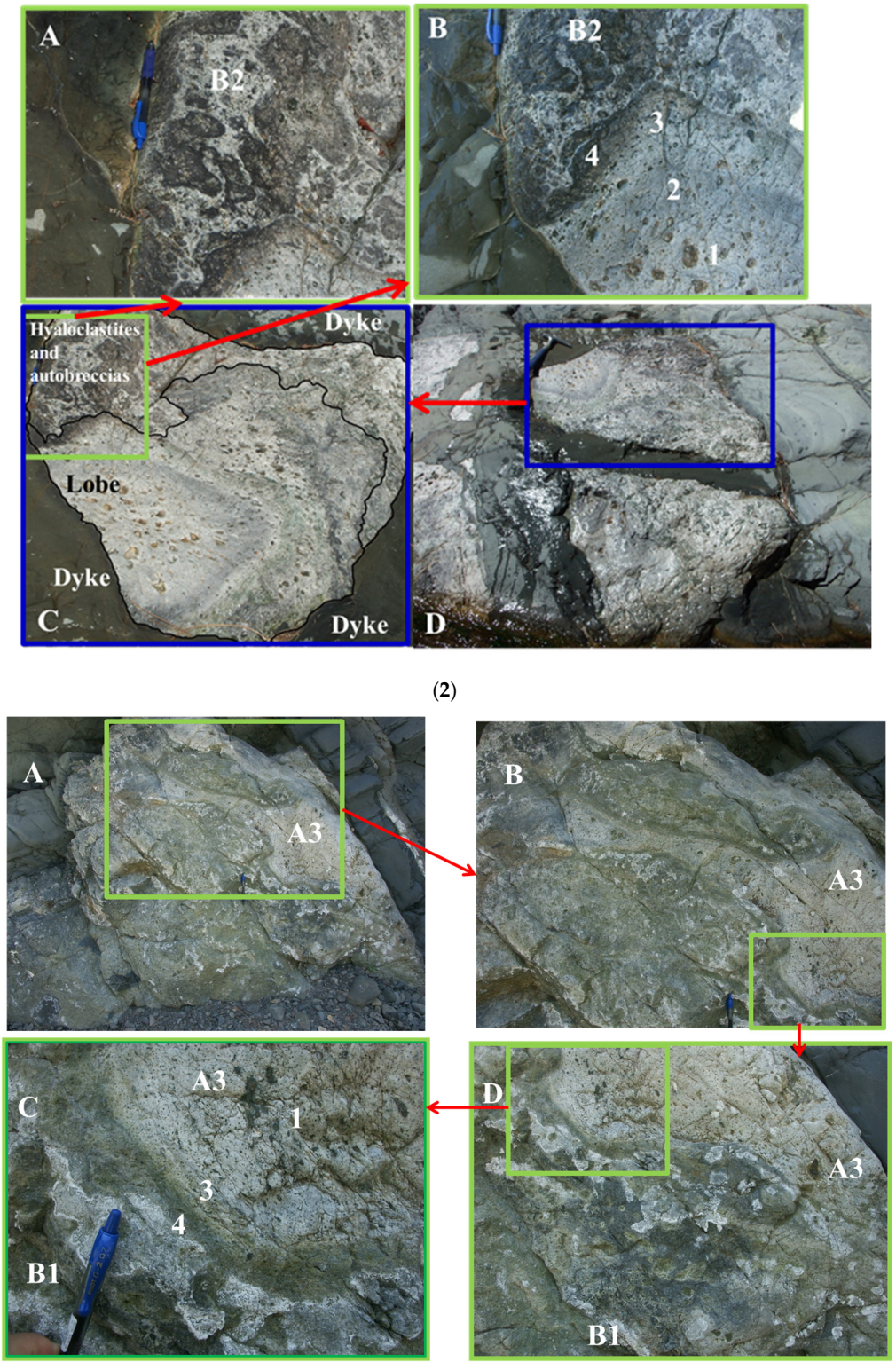

Figure 4. *Cont.*

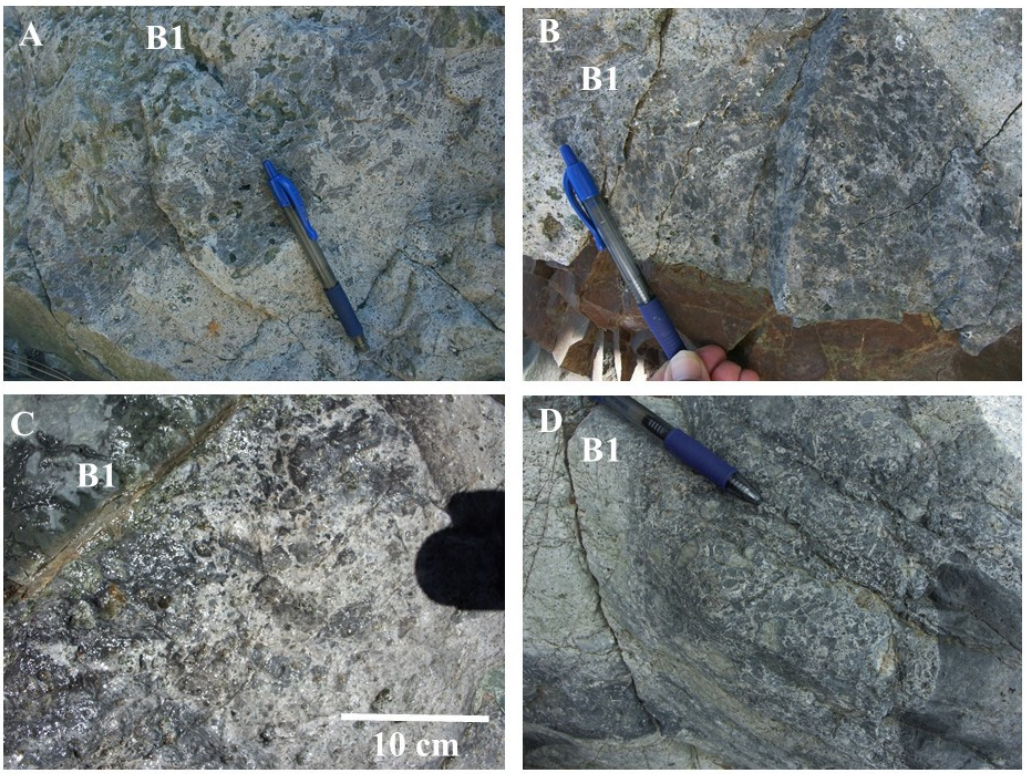

(**4**)

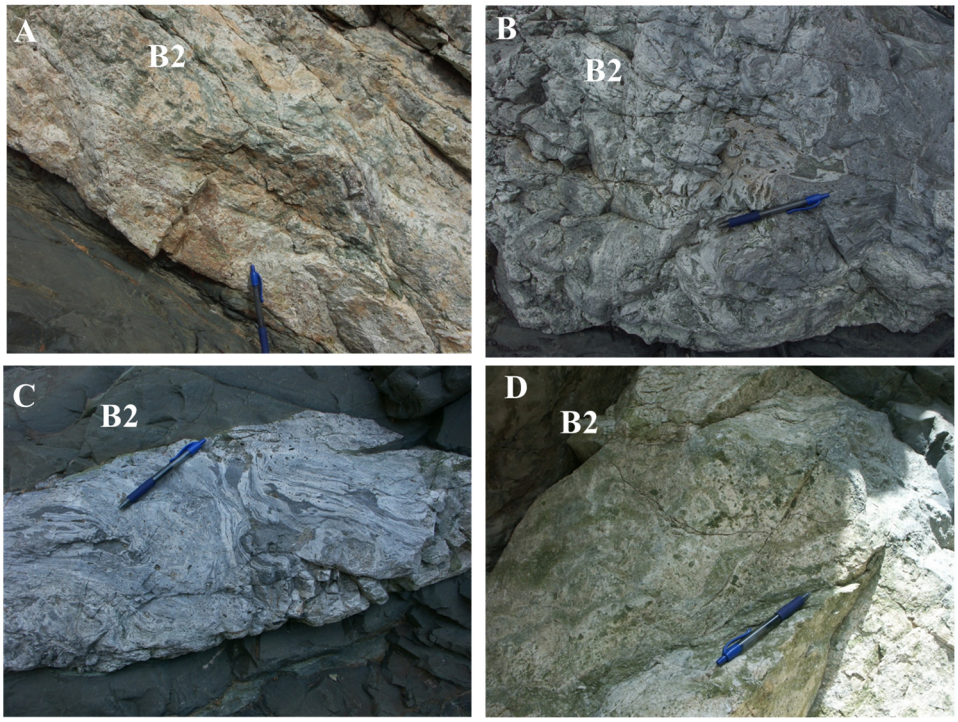

(**5**)

Figure 4. *Cont*.

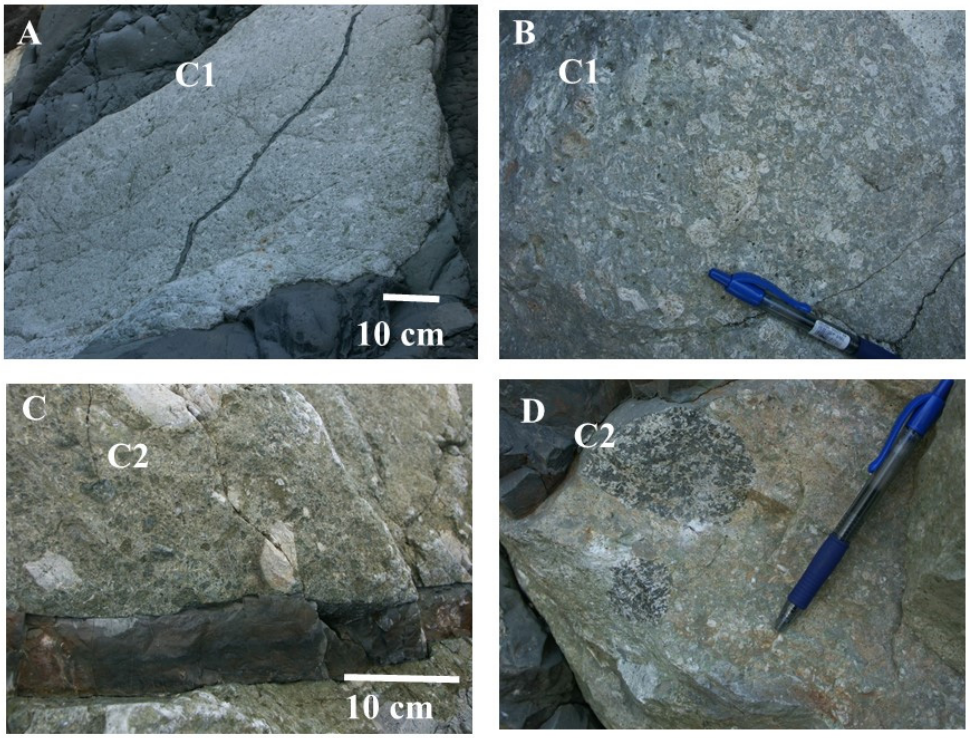

(**6**)

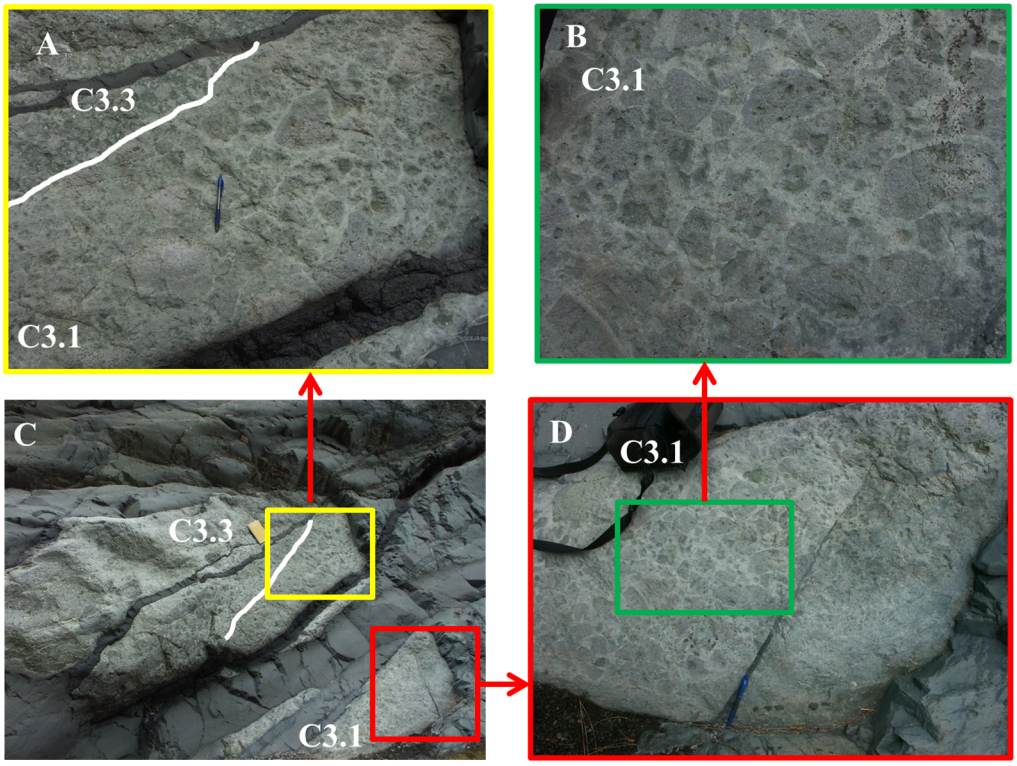

(**7**)

Figure 4. *Cont*.

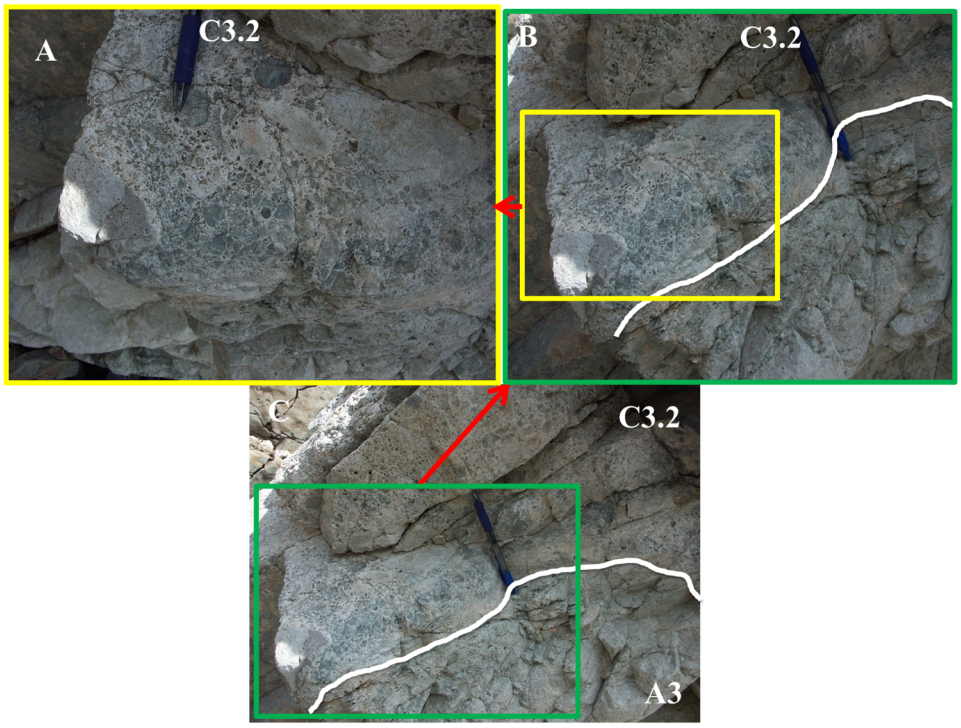

(**8**)

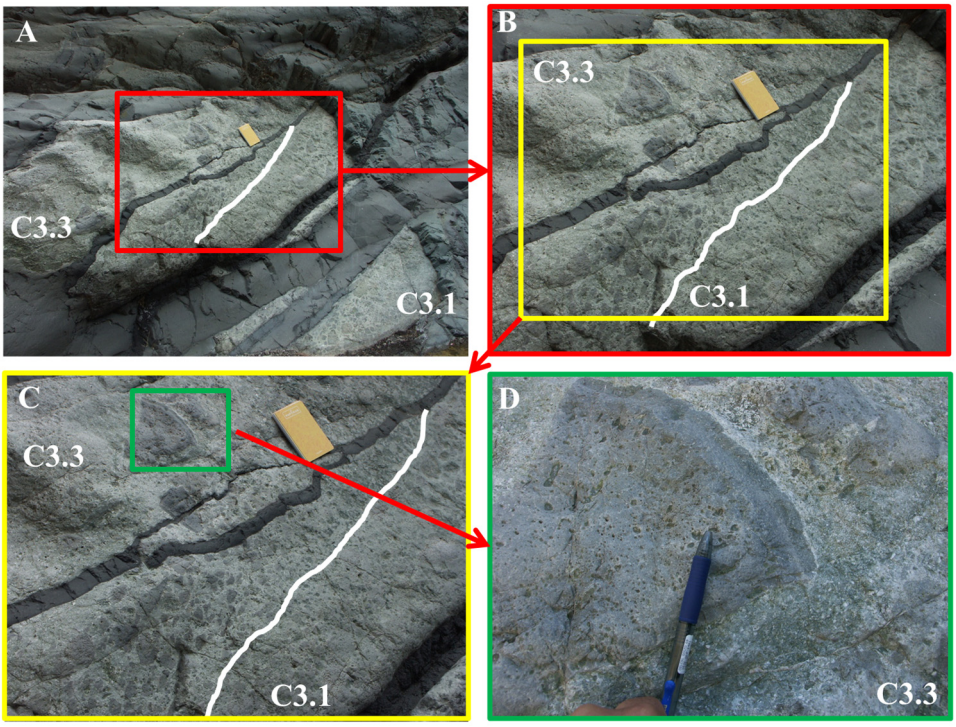

(**9**)

Figure 4. *Cont*.

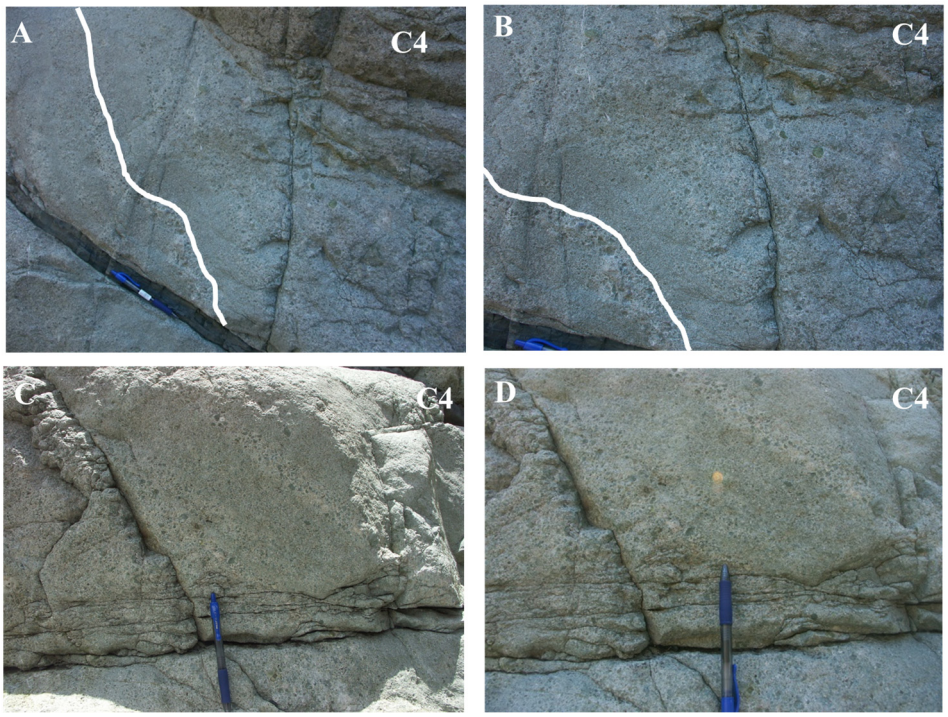

(**10**)

Figure 4. (**1**) The appearance of lithofacies A1 (trachybasaltic pillow lavas). The morphology of the pillow lavas is visible in (A, B, C). Detail of a pillow lava (D). (**2**) The appearance of lithofacies A2 (lobes of vitreous or aphanite trachytes; the photos A, B, C, D show the lobe at different scales and details of the different parts of the lobe and its surroundings). The explanation of numbers 1, 2, 3, and 4 is found in Table 1. B2 is an autobreccia. (**3**) The appearance of lithofacies A3 (lobes of porphyritic trachytes; the photos A, B, C, D show the lobe at different scales and details of the different parts of the lobe and its surroundings). The explanation of numbers 1, 3, and 4 is found in Table 1. B1 is a hyaloclastite. (**4**) The appearance of lithofacies B1 (hyaloclastites; the photos A, B, C, and D show different aspects of hyaloclastites). (**5**) The appearance of lithofacies B2 (autobreccias; the photos A, B, C, and D show different aspects of autobreccias). (**6**) (A, B) The appearance of lithofacies C1 (trachyte breccias, massive or with slight normal grading). (C, D) The appearance of facies C2 (polymictic massive breccias). D shows rounded fragments of plutonic rocks. (**7**) The appearance of lithofacies C3.1. (polymictic massive breccias with inverse grading at the base; the photos A, B, C, and D show different aspects of the polymictic massive breccias with inverse grading at the base). White lines mark the bedding. The explanation of the facies C3.1 and C.3.3 is found in Table 1. (**8**) The appearance of lithofacies C3.2. (polymictic massive breccias with inverse grading at the base; the photos A, B, C, show the polymictic massive breccias with inverse grading at different scales and details of the different parts of the breccia and its surroundings). White lines mark the bedding. The explanation of the facies C3.2 is found in Table 1. A3 is a lobe of porphyritic trachytes. (**9**) The appearance of lithofacies C3.3. (polymictic massive breccias with inverse grading at the base; the photos A, B, C, and D show different aspects of the polymictic massive breccias with inverse grading at the base). White lines mark the bedding. The explanation of the facies C3.1 and C3.3 is found in Table 1. (**10**) The appearance of lithofacies C4 (polymictic sandstones and breccias with inverse grading at the base). (B) is a detail of (A), and (D) is a detail of (C). White lines mark the bedding. The colored boxes and arrows indicate the position of the different detail photographs.

3.2. Meaning of the Submarine Felsic Episode

The features of the facies described above and their arrangement in the felsic episode suggest that this unit of the La Palma submarine edifice represents a trachytic lobe–hyaloclastite complex (see Figure 5) similar to those described by [217–219]. So far, they have only been described in modern mid-ocean ridges, in ophiolitic complexes such as Oman and Semail,

and in subduction areas in arc-island and back-arc environments [221] (for example, Canadian Archean and subglacial Quaternary rhyolites in Iceland), making the La Palma case the first example described in oceanic islands with an intraplate environment.

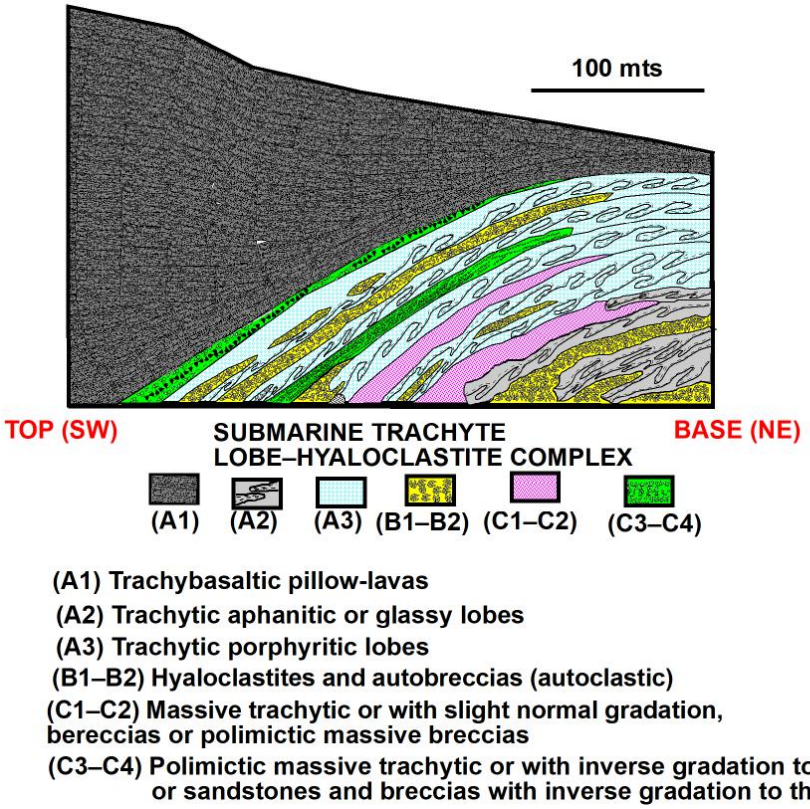

Figure 5. The general internal structuring of the lobe–hyaloclastic complex of La Palma. Neither gabbros nor intrusive dykes are shown.

These complexes represent the final, most evolved, and least voluminous episodes of the evolution of basaltic fissure volcanism that forms large shield volcanoes on the ocean floor. They usually infill collapse calderas formed in the highest part of these volcanoes [217–219] and comprise several facies interpreted to represent the near-vent innermost part to the distal, outermost parts. These are as follows:

(1) Massive proximal deposits with densely stacked lobes more than 100 m long, which start from a central feeder dam, arranged down the slope, and which, due to their higher viscosity and lower temperature, differ in shape from the lobes of basaltic and trachybasaltic flows (pillow lavas).

(2) The middle zone of hyaloclastite lobes: 2–100 m long lobes surrounded by hyaloclastite and brecciated lavas with flow banding.

(3) The distal breccia zone: hyaloclastitic matrix-supported breccia with lobe clasts and few brecciated lobes with "jigsaw-fit" or clast-rotated textures. Two types of breccias are distinguished: (a) autobreccias forming a shell that overlies the lobes (clasts with flow bands in a chaotic arrangement) and (b) hyaloclastitic flank breccias (clast-supported, with large fragments of lobes, interspersed with stratified hyaloclastites) that form the distal and lateral edges of the complex (flank breccias). The genesis of the latter is due to the late sliding and repositioning of autobreccias and hyaloclastites by submarine mass flows.

3.3. Geochemical Study of the Trachytic Lobe–Hyaloclastite Complex

A total of fifteen new whole-rock chemical analyses (Table S1) were performed on the volcanic rocks from the submarine lobe–hyaloclastite complex exposed in the Caldera de Taburiente. Ten of these samples correspond to the coherent trachytic facies (TAB-06, TAB-30B, TAB-23, TAB-33A, TAB-33B, TAB-45, TAB-16, TAB-36, TAB-40, and TAB-41), while five samples correspond to the dykes of intermediate composition (TAB-08, TAB-34, TAB-42, TAB-43, and TAB-47) that intrude the trachytic lobe–hyaloclastic complex. The first four dykes are interpreted as coeval with the submarine phase, whereas TAB-47 is related to the younger subaerial volcanic activity. In addition, six samples from the younger submarine basaltic–trachybasaltic sequence were analyzed (TAB-28B, TAB-29B, TAB-49, TAB-50, TAB-51, and TAB-52).

In the TAS diagram (Figure 6A), the rocks of the lobe–hyaloclastite complex are plotted as trachytes and constitute the series of rocks with the highest silica saturation on the island (60 to 67 wt.% SiO_2). In contrast, the rocks of the youngest and less differentiated submarine volcanic formation and the earliest intermediate dykes of the Basal Complex define a compositional trend, from basalts and trachybasalts (hawaiites) to mugearitic and benmoreitic compositions [226]. The dyke associated with subaerial volcanism (hollow green triangle in Figure 6A) projects near the tephryphonolite field, reflecting its undersaturated nature. For this reason, it is excluded from further geochemical interpretations. Within the trachyte field, a distinction is evident between aphanitic and porphyritic types. The aphanitic trachytes (filled triangles) appear slightly more evolved than the porphyritic ones (hollow triangles).

Despite showing relatively low LOI proportion (<2.5% in most cases), mineralogical evidence confirms substantial hydrothermal alteration in the La Palma submarine trachytes, particularly an intense albitization of potassium feldspar [129]. This alteration is reflected in unusually low K_2O contents (<0.35%) compared to other Canary Island trachytes. As a result, the rocks of the lobe–hyaloclastite complex must be considered meta-trachytes.

Trachytes from the Basal Complexes (B.C.) of La Palma, La Gomera, and Fuerteventura (Figure 6B) occupy similar positions in the TAS diagram and exhibit notable K_2O deficiencies. However, the closest compositional analogs to the La Palma submarine trachytes are found in the unaltered trachytes of the Henry Seamount [227], the xenopumices from the 2011–2012 El Hierro eruption [228], and the less altered pumice emitted as enclaves in the Teneguía eruption in 1971; none of which show signs of hydrothermal alteration. When projected onto the diagram proposed by [229] (Figure S2), porphyritic trachytes fall into the phonolite field, while aphanitic trachytes are projected onto the boundary between phonolite and trachyte.

Since the trachytes of the lobe–hyaloclastite complex in the Caldera de Taburiente predate the overlying submarine basaltic–trachybasaltic rocks, with which they exhibit clear stratigraphic continuity, it is reasonable to consider a possible genetic link via fractional crystallization. However, it is difficult to reconcile such a scenario, as it would require the early eruption of highly differentiated magmas followed—after an undefined interval—by the emplacement of basaltic melts that are compositionally closer to primary magmas, despite their spatial and temporal association.

To investigate the petrogenetic processes responsible for the formation of the submarine rocks of the Basal Complex (B.C.), a trace element analysis was conducted across the various lithological units. In particular, binary diagrams using pairs of highly incompatible elements (CiH–CjH; [230]) can effectively test whether these rocks are genetically related through fractional crystallization processes.

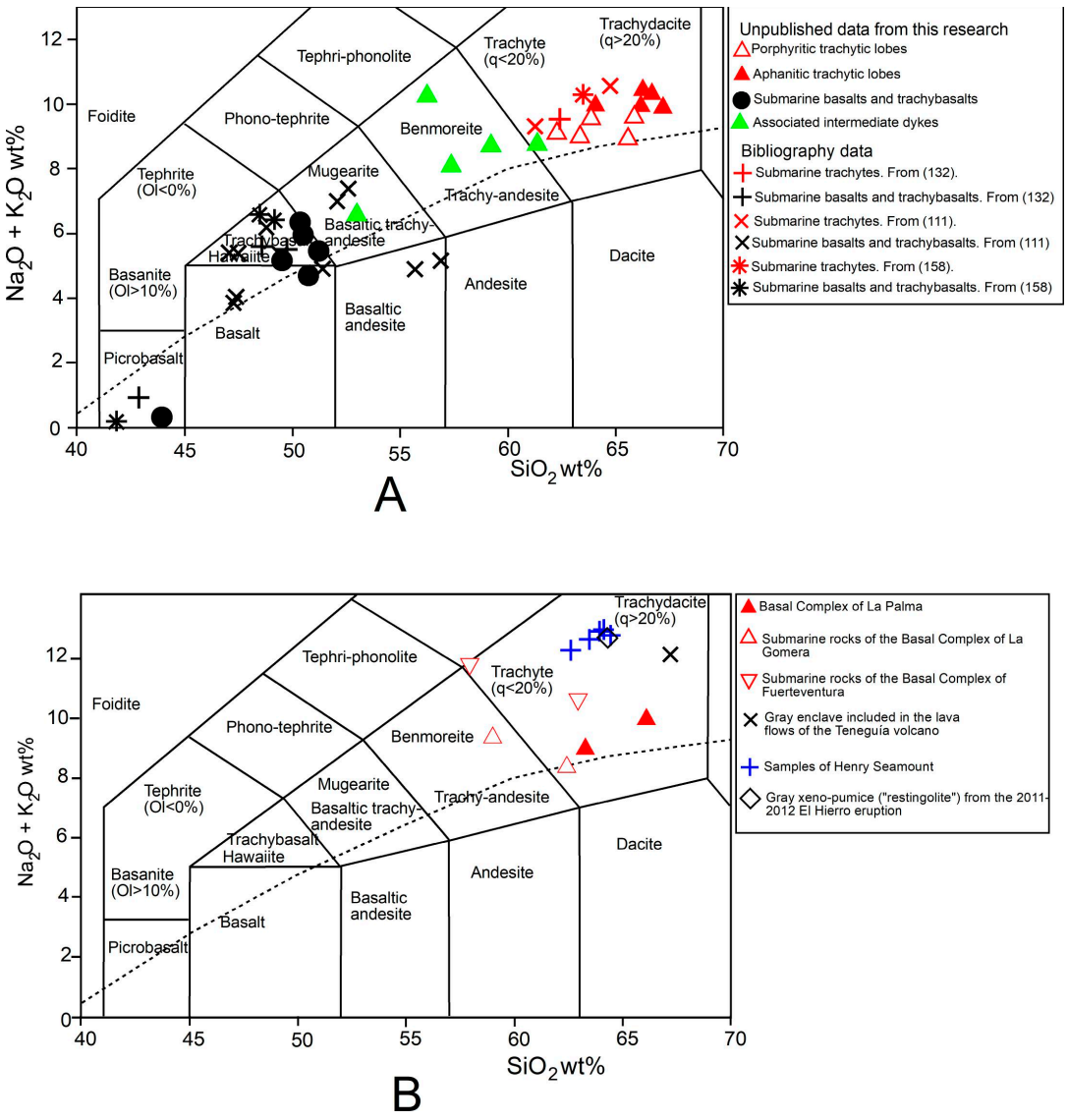

Figure 6. A TAS diagram of submarine volcanic rocks and xenoliths from the Canary Islands. (**A**) Samples from the submarine formation of La Palma. Symbols: black-filled circles—basaltic and trachybasaltic rocks (this work); green—intermediate dykes; red—trachytic lobes; crosses—data from [132]; Xs—data from [108]; asterisks—data from [154]; additional symbols from this work: hollow triangles—porphyritic trachytes; filled triangles—aphanitic trachytes. (**B**) Selected trachytes from various Canary Island sources. Symbols: filled triangles—Basal Complex (B.C.) of La Palma; hollow triangles—submarine rocks from the B.C. of La Gomera; inverted triangles—submarine rocks from the B.C. of Fuerteventura; X—gray enclave included in lava flows of the 1971 Teneguía eruption; crosses—samples from Henry Seamount; rhomb—gray xenopumice ("restingolite") from the 2011–2012 El Hierro eruption.

For example, in the La–Th and Ce–Nb diagrams (Figure 7), the trachytes of the lobe–hyaloclastite complex plot along one linear trend, while the younger submarine basaltic–trachybasaltic rocks and the earliest intermediate dykes that intrude the complex define a separate trend. Both trends originate from the diagram's origin, suggesting that they represent distinct fractional crystallization series derived from different primary magmas.

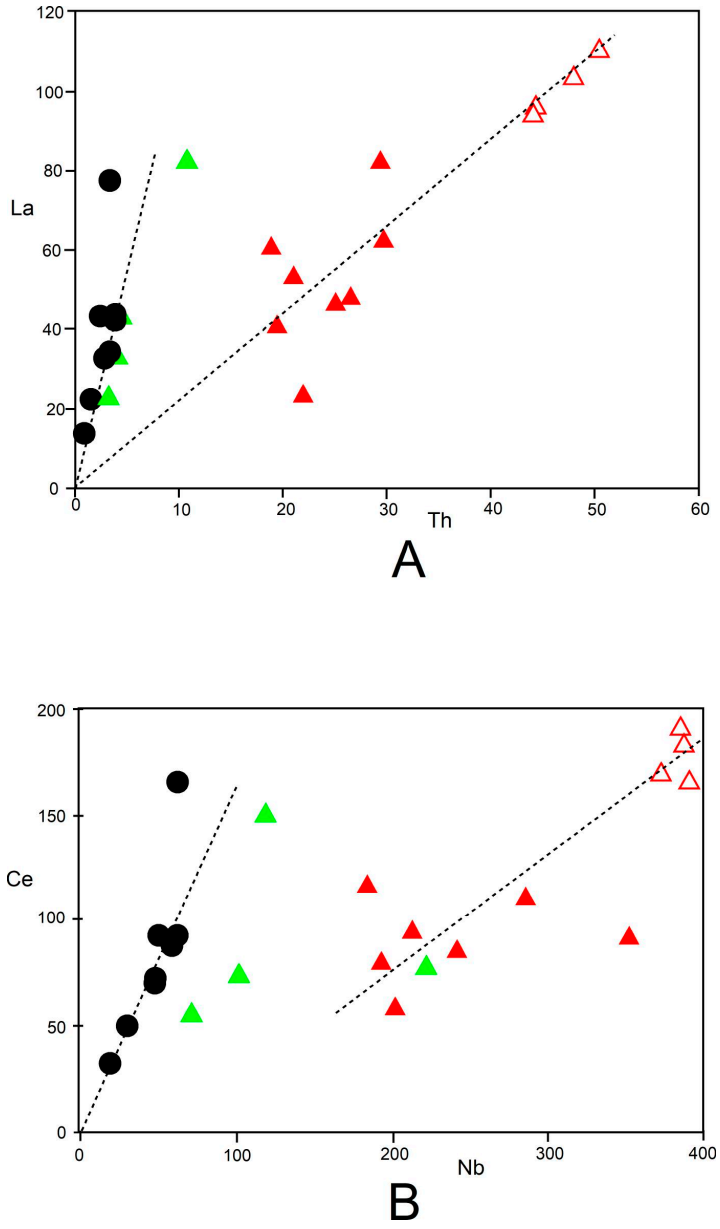

Figure 7. Diagrams of incompatible elements CiH-CjH. (**A**) Th-La (in ppm). (**B**) Nb-Ce (in ppm). Symbols as in Figure 6A.

This implies that the trachytes represent the final differentiated products formed from different fractional crystallization processes, possibly from different primary magmas. This way, the trachytes of the lobe–hyaloclastitic complex would be the final terms of a series of magmatic differentiation formed by the fractional crystallization of older and different basaltic magmas to those that subsequently gave rise to later submarine basaltic and trachybasaltic rocks, outcroppings in the B.C. from La Palma. Furthermore, in the Nb–Ce diagram, the trachytes form a linear trend that does not pass through the origin (Figure 7B), indicating the likely involvement of apatite during the crystallization process.

Although some overlaps exist, the overall distribution in Figure 7 suggests that the mugearitic and benmoreitic dykes crossing the trachytic complex may have originated from the fractional crystallization of the magmas responsible for the younger submarine basaltic–trachybasaltic rocks.

A similar conclusion is supported by the analysis of CiH–CiH/CjH-type diagrams [230], such as Th vs. Th/La and Ta vs. Ta/La. If the trachytes of the lobe–hyaloclastite

complex were genetically related to the magmas that produced the submarine basalts and trachybasalts through fractional crystallization, both groups would be expected to plot along a horizontal line, parallel to that defined by the mugearitic and benmoreitic dykes (as illustrated by the dashed line in Figure 8). However, this pattern is not observed. Instead, the trachytes—both aphanitic and porphyritic—plot along a distinct linear trend parallel to the X-axis but originating from higher Th/La and Ta/La ratios (the solid line in Figure 8). This suggests that the trachytes were derived from the fractional crystallization of older basaltic magmas with higher initial Th/La and Ta/La values than those that later produced the submarine basaltic–trachybasaltic rocks and their associated dykes.

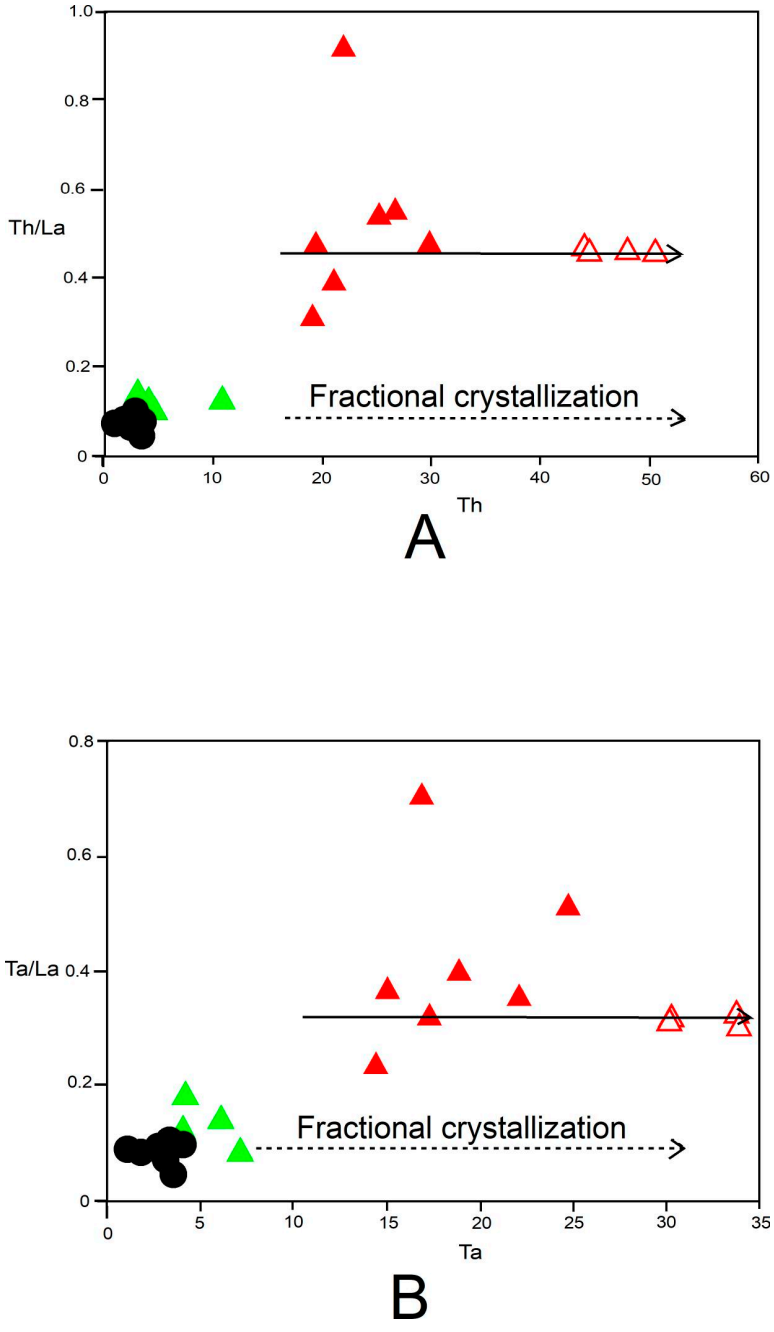

Figure 8. Diagrams of incompatible CiH-CiH/CjH elements. (**A**) Th-Th/La and (**B**) Ta-Ta/La. Symbols as in Figure 6A.

All the rocks of the La Palma submarine volcanic edifice have been represented in a diagram of incompatible trace elements normalized to the primitive mantle [231] (Figure 9).

This diagram shows that trachytic rocks show strong depletion in Rb, Ba, K, Sr, Eu, P, and Ti. Depletion in some of these incompatible elements (Rb, K, and, probably, Ba) can be explained by the remobilization due to the action of hydrothermal metamorphism that has mainly affected the trachytes, as they are the most ancient and located more towards the center of the volcanic edifice, where warming was greater due to the greater intensity of the plutonic and dyke intrusion. Depletion in the rest of these elements (Sr, Eu, P, and Ti) indicates the intervention of fractional crystallization processes in the trachytic magmas of minerals such as plagioclase (Sr, Eu), ilmenite–sphene (Ti), or apatite (P) [232], fractionation that is not appreciated to have affected the magmas that gave rise to the mugearitic–benmoreitic dykes that cross the trachytes. On the other hand, the trachytes (and the dykes) also show an enrichment in Th, U, Nb, and Zr, characteristic of differentiated rocks.

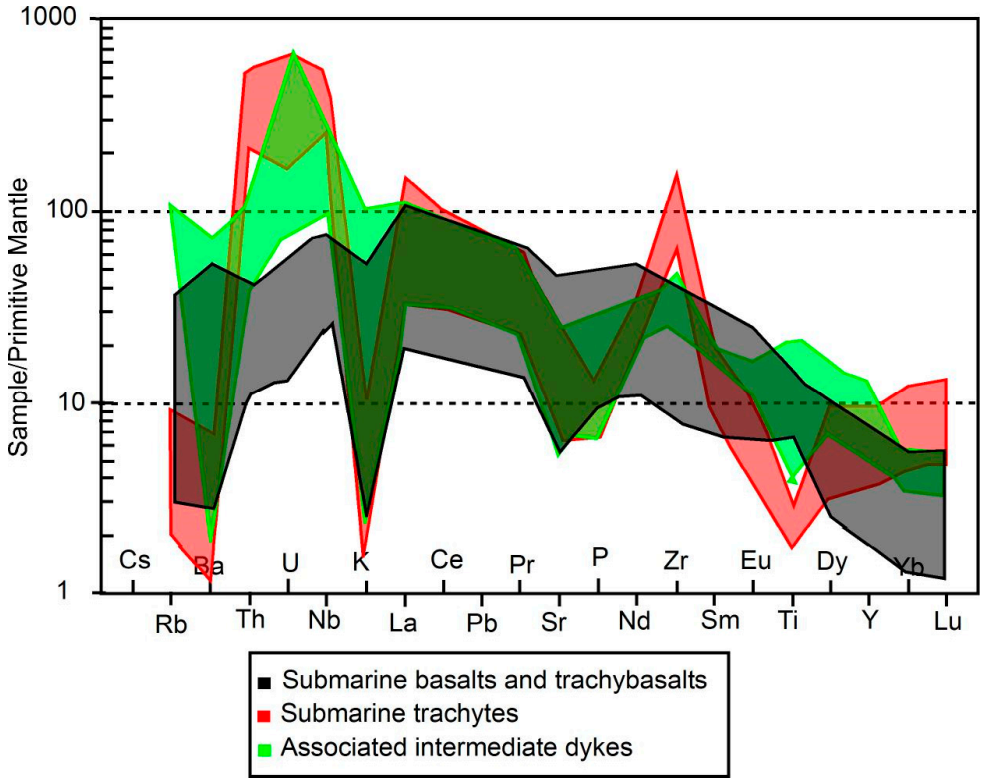

Figure 9. Diagram of incompatible trace elements normalized to primitive mantle [231] of submarine basalts and trachybasalts (black, 1), submarine trachytes (red, 2), and associated intermediate dykes (green, 3).

In the rare earth element diagram normalized to the primitive mantle [231], the composition of the submarine rocks of La Palma BC (Figure 10) reveals the following:

1. The trachytes do not exhibit significant enrichment in light rare earth elements compared to the basaltic–trachybasaltic rocks, supporting the interpretation that the two are not genetically related.
2. The trachytes display a marked depletion in intermediate rare earth elements (MREEs), consistent with the fractional crystallization of sphene and apatite—an observation that aligns with the Ti and P depletion shown in Figure 9. The negative Eu anomaly in the trachytes suggests fractional crystallization of plagioclase during the differentiation process. In contrast, the mugearitic and benmoreitic dykes that intrude the trachytes do not show this MREE depletion. Instead, they exhibit slight MREE enrichment, further indicating that they are not cogenetic with the trachytes of the lobe–hyaloclastite complex.

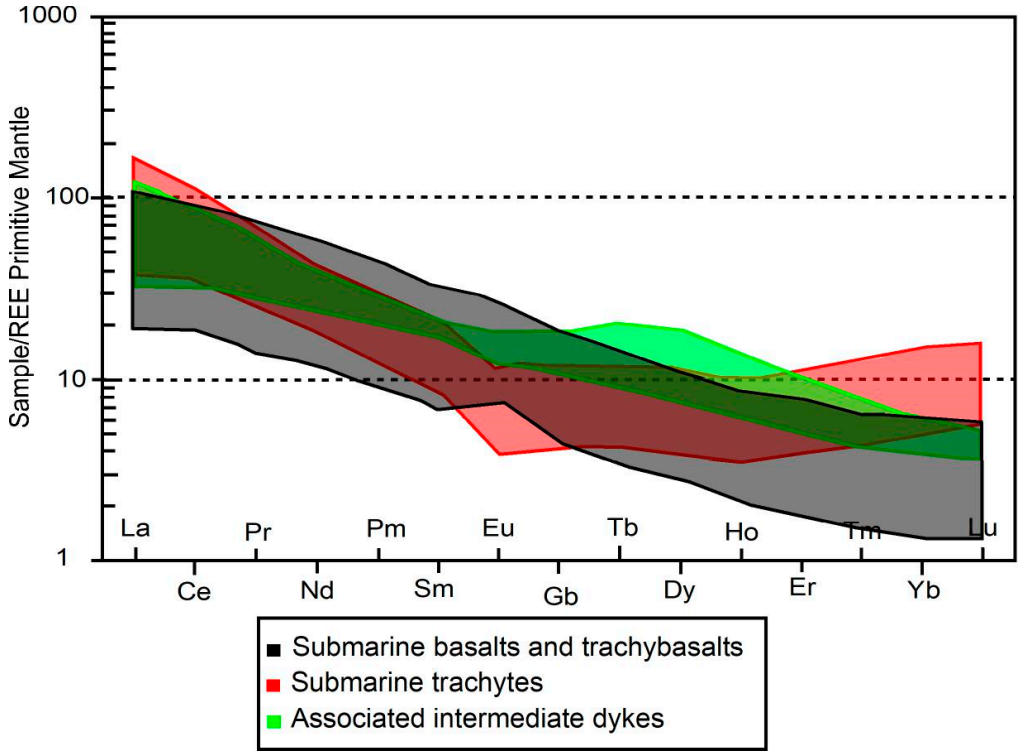

Figure 10. Rare Earth Diagram normalized to the primitive mantle [233].

In summary, the combined analysis of incompatible trace elements and REE patterns in the submarine rocks of the La Palma Basal Complex and in the earliest intermediate dykes confirms the absence of a genetic relationship between the trachytes of the lobe–hyaloclastitic complex and the rest of the submarine volcanic formation of La Palma. The trachytic lobe–hyaloclastite complex is, therefore, interpreted to be the product of an earlier submarine basaltic magmatic episode, not exposed on the island nowadays.

3.4. Age of the Lobe–Hyaloclastite Rocks Complex

Four trachyte samples from the lobes of the submarine lobe–hyaloclastite complex were collected at different stratigraphic levels along the Barranco de las Angustias (samples TAB-12, TAB-23, TAB-24, and TAB-33B). Their positions are indicated in Figure 2.

Table 2 presents the ages obtained using the U–Pb method on zircons from several trachyte samples (see Table S2 and Figure S3). The resulting age for the trachytes is approximately 3.10 ± 0.03 Ma.

Table 2. U-Pb ages on zircons from rocks of the La Palma trachyte submarine lobe–hyaloclastitic complex. The position of the samples appears in Figure 2. The average of the four U-Pb concordia ages indicates an extrusion/crystallization age of 3.10 ± 0.03 Ma.

Sample	Chemical Classification	Position	N (N° of the Zircon Crystals)	Concord $^{206}Pb/^{238}U$ (207 Corrected)	Age (Ma)
TAB-12	Trachyte	Las Angustias ravine (380 mts height)	20	3.08 ± 0.1	3.10 ± 0.03
TAB-23	Trachyte	Las Angustias ravine (380 mts height)	19	3.14 ± 0.05	
TAB-24	Trachyte	Las Angustias ravine (360 mts height) (El Carbón)	20	3.13 ± 0.05	
TAB-33B	Trachyte	Las Angustias ravine (390 mts height)	20	3.06 ± 0.1	

This age is consistent with that yielded by foraminifera collected from hyaloclastite layers in the upper part of the overlying submarine basaltic rocks, which ranges between 2.8 and 4 Ma [109,184].

One trachybasalt sample (A1 facies in Table 1), collected from pillow lavas at an elevation of 340 m above sea level in the stratigraphic section of the Barranco de las Angustias (sample TAB-28B, see Figure 2), has been dated.

Table 3 presents the age obtained via the ^{40}Ar-^{39}Ar method on amphibole from this trachybasalt sample (see Table S3 and Figure S4). The resulting age is 2.48 ± 0.15 Ma, being consistent with its stratigraphic position above the trachytic submarine lobe–hyaloclastite complex.

Table 3. ^{40}Ar-^{39}Ar ages on amphibole from trachybasaltic pillow lavas (A1 unit of Table 1). The position of the sample is shown in Figure 2.

			Age (Ma)		
Sample	Chemical composition	Position	Normal isochron	Inverse isochron	Weighted plateau
TAB-28 (amphibole)	Trachybasalt	Las Angustias ravine (340 mts height) (El Carbón)	2.49 ± 0.33	2.48 ± 0.32	2.48 ± 0.15

However, this age is younger than that (2.8–4 Ma) yielded by the foraminifera from the hyaloclastite layers overlying the trachytes [109,184] mentioned previously.

Accurate determination of the age of the oldest volcanic rocks exposed on La Palma—identified in this study as the trachytic submarine lobe–hyaloclastite complex—allows us to establish a minimum age of 3.1 Ma for the onset of submarine growth of the island.

This precise chronological marker provides a valuable constraint for testing age progression models across the Canary Archipelago. These models can shed further light for evaluating the validity of competing theories regarding the origin and evolution of the archipelago.

3.5. Significance of the La Palma Trachyte Submarine Lobe–Hyaloclastitic Complex in the Regional Context of the Canary Islands

Felsic submarine volcanic rocks have also been identified on other islands of the Canary Archipelago, associated with the stages of submarine growth and early subaerial emergence. On La Gomera, for example, trachyte breccias related to submarine volcanism are present in the Basal Complex of the island [124,126,127,159,234], although their significance remains unclear. On Fuerteventura, both the Submarine Volcanic Group and the Transitional Volcanic Group, as defined by [115], include coherent bodies and associated breccias of trachytic or phonolitic composition. These could represent lobe–hyaloclastitic complexes analogous to the one described in this study for La Palma.

In addition, ref. [233] reported several dated samples of felsic volcanic rocks—trachytes and phonolites—from seamounts near the Canary Islands. At Hierro Ridge, K-feldspar and hornblende from a trachyte breccia yielded ages of 133.3 ± 0.2 Ma and 133.8 ± 0.6 Ma, respectively. In the Bisabuelas Seamounts, plagioclase in trachyte was dated between 140.5 ± 0.7 Ma and 141.7 ± 0.4 Ma. At The Paps Seamount, K-feldspar from a trachyphonolitic pumice breccia returned an age of 91.1 ± 0.2 Ma. Finally, at Tropic Seamount, K-feldspar, plagioclase, and anorthoclase from trachyte samples were dated at 119.3 ± 0.3 Ma, 115.6 ± 0.5 Ma, and 116.3 ± 0.2 Ma, respectively. These felsic rocks may also represent lobe–hyaloclastitic complexes similar to the one documented on La Palma.

In this context, ref. [233] also dated biotite crystals from phonolites forming part of the La Palma Ridge—a seamount located on the southern submarine flanks of La Palma—obtaining an age of 2.11 ± 0.03 Ma. This age is younger than that of the uplifted seamount series exposed in northern La Palma and analyzed in this study.

The occurrence of felsic volcanic rocks both in the submarine sequences of several Canary Islands (La Palma, La Gomera, and Fuerteventura) and in nearby seamounts

provides compelling evidence that seamount formation in the region alternated between episodes of more basic, basaltic volcanism (sensu lato) and phases characterized by more differentiated, felsic magmatism, in this case, trachytic and phonolitic.

4. Conclusions

The submarine volcanic rocks of the La Palma Basal Complex comprise two distinct units—an older felsic formation and a younger conformable basaltic–trachybasaltic formation—indicating clear stratigraphic continuity. The felsic unit is composed of porphyritic, aphanitic, and vitreous trachytes and includes three main types of facies: (A) coherent facies forming trachytic lobes; (B) autoclastic facies, such as hyaloclastites and autobreccias; and (C) syn-eruptive resedimented facies, which consist of massive or graded, mono- and polymictic breccias, as well as volcaniclastic sandstones and breccias.

The overall structural and stratigraphic organization of these facies is consistent with a submarine trachytic lobe–hyaloclastite complex that predates the overlying basaltic–trachybasaltic sequence.

The analysis of incompatible trace elements indicates that fractional crystallization can account for the diversity of trachytic facies observed, specifically, the porphyritic and aphanitic trachytes. Moreover, the data demonstrates a lack of genetic relationship between the magmas that produced these trachytic facies and those responsible for the formation of the overlying submarine basaltic and trachybasaltic rocks, which also belong to the La Palma Basal Complex. The trachytic magmas that formed the lobe–hyaloclastite complex likely represent the final evolutionary products of an earlier submarine basaltic edifice, no longer exposed on the island.

Geochronological data obtained from U–Pb zircon dating support this interpretation. Given that the trachytic lobe–hyaloclastite complex is the oldest exposed rock unit on La Palma, a minimum age of approximately 3.10 Ma is proposed for the beginning of the island's submarine volcanic growth.

Supplementary Materials: The following supporting information can be downloaded at: https://www.mdpi.com/article/10.3390/min15101007/s1, Figure S1: The images of the zircon grains analyzed (by cathodoluminescence in transmitted and reflected light). Figure S2: Diagram of Nb/Y-Zr/TiO_2, which represents the chemical composition of the aphanitic and porphyritic trachytes (same symbology as Figure 6). Figure S3: Concordia diagrams showing SHRIMPI zircon analyses from the trachyte lobes of the submarine trachytic lobe–hyaloclastite complex of the Caldera of Taburiente. Figure S4: Ar–Ar data (TAB-28B) for an amphibole crystal included in trachybasalt pillow lava. This figure shows the weighted plateau age and normal/inverse isochron diagrams for the ^{40}Ar–^{39}Ar age data. Table S1: Rock analyses of the studied Fuerteventura rocks. Table S2: U–Pb SHRIMP data of zircons for samples TAB-12, TAB-23, TAB-24, and TAB-33B from the trachyte lobes of the submarine trachytic lobe–hyaloclastite complex of the Caldera of Taburiente. Table S3: Ar–Ar data (TAB-28B) for an amphibole crystal included in trachybasalt pillow lava.

Author Contributions: Conceptualization: R.C., J.d.l.N., J.R.C., and C.F.; methodology: R.C., J.d.l.N., J.R.C., C.F., F.J., S.H. and R.L.; software: R.C. and J.d.l.N.; fieldwork and sampling: R.C., J.d.l.N., J.R.C. and C.F.; validation of results: R.C., J.d.l.N., J.R.C. and C.F.; formal analysis: F.J., S.H. and R.L.; investigation: R.C., J.d.l.N., J.R.C., C.F., F.J., S.H. and R.L.; resources: R.C., F.J., S.H. and R.L.; data curation: R.C., J.d.l.N. and J.R.C.; writing—original draft preparation: R.C. and J.d.l.N.; writing—review and editing: R.C., J.d.l.N., J.R.C., C.F., F.J., S.H. and R.L.; visualization: R.C. and J.d.l.N.; supervision: R.C., J.d.l.N., J.R.C. and C.F.; project administration: R.C.; funding acquisition: R.C. All authors have read and agreed to the published version of the manuscript.

Funding: This research was funded by projects CGL 2006-00970/BTE, CGL2009-07775, CGL2016-75062-P, and PID2020-112920GB-I00 of the Spanish Ministry of Education and Science, the Spanish Ministry of Science and Innovation, the Spanish Ministry of Science Innovation; and the Universities,

and Spanish Ministry of Science and Innovation, respectively; from project 2008/0250 (Canary Islands Agency for Research, Innovation and Information Society of the Government of the Canary Islands); from project PIL2190901 of the Government of the Canary Islands; from project 529/2012 of the Autonomous Body of National Parks of the Spanish Ministry of Agriculture, Food and Environment; from an Integrated Action between Hungary and Spain (HH2004-0027 and MEC E-38/01, E-22/04); and the International Complementary Action PCI2006-A7-0520 of the Spanish Ministry of Education and Science is gratefully acknowledged. This work is also supported by the MTA–HUN-REN CSFK Lendület "Momentum" PannonianVolcano Research Group (LP2024-9/2024).

Data Availability Statement: The authors confirm that the data supporting the findings of this study are available within the article and its Supplementary Materials.

Acknowledgments: We thank Ángel Palomares from Caldera de Taburiente National Park, and the rest of the Park staff, especially Álvaro Rodríguez and Valentín Abel Rodríguez. We also thank Gloria Martín Velázquez for her collaboration in field activities. We would also like to thank Jocelyn McPhie for her ideas and comments that helped improve the manuscript. We express our gratitude to the four anonymous reviewers of the article, as well as to the guest editor (Enrique Merino Martínez (IGME-CSIC)), for their comments and suggestions that have enriched the content and format of the article. We thank Luciana P. Pereira for her suggested English corrections. This is an IBERSIMS publication No. 127.

Conflicts of Interest: The authors declare that there is no conflicts of interest.

References

1. Morgan, W.J. Convection Plumes in the Lower Mantle. *Nature* **1971**, *230*, 42–43. [CrossRef]
2. Troll, V.R.; Deegan, F.M.; Burchardt, S.; Zaczek, K.; Carracedo, J.C.; Meade, F.C.; Soler, V.; Cachao, M.; Ferreira, J.; Barker, A.K. Nannofossils: The smoking gun for the Canarian hotspot. *Geol. Today* **2015**, *31*, 137–145. [CrossRef]
3. Hoernle, K.; Schmincke, H.U. The role of partial melting in the 15-Ma geochemical evolution of Gran Canaria: A blobmodel for the Canary hotspot. *J. Pet.* **1993**, *34*, 599–626. [CrossRef]
4. King, S.D.; Ritsema, J. African hot spot volcanism: Small-scale convection in the upper mantle beneath cratons. *Nature* **2000**, *290*, 1137–1140. [CrossRef]
5. Geldmacher, J.; Hoernle, K.; Bogaard, P.V.D.; Duggen, S.; Werner, R. New $^{40}Ar/^{39}Ar$ age and geochemical data from seamounts in the Canary and Madeira volcanic provinces: A contribution to the "Great Plume Debate". *Earth Planet. Sci. Lett.* **2005**, *237*, 85–101. [CrossRef]
6. Gurenko, A.A.; Hoernle, K.A.; Sobolev, A.V.; Hauff, F.; Schmincke, H.U. Source components of the Gran Canaria (Canary Islands) shield stage magmas: Evidence from olivine composition and Sr-Nd-Pb isotopes. *Contrib. Mineral. Petrol.* **2010**, *159*, 689–702. [CrossRef]
7. Anguita, F.; Hernán, F. A propagating fracture model versus a hot-spot origin for the Canary Islands. *Earth Planet. Sci. Lett.* **1975**, *27*, 11–19. [CrossRef]
8. Araña, V.; Ortiz, R. The Canary Islands: Tectonics, magmatism and geodynamic framework. In *Magmatism in Extensional Structural Settings: The Phanerozoic African Plate*; Kampunzu, A.B., Lubala, R.T., Eds.; Springer: New York, NY, USA, 1991; pp. 209–249.
9. Anguita, F.; Hernán, F. The Canary Islands origin: A unifying model. *J. Volcanol. Geotherm. Res.* **2000**, *103*, 1–26. [CrossRef]
10. Anguita, F.; Fernández, C.; Márquez, Á.; Álvarez-León, R.; Casillas, R. The Canary hotspot revisited: Refutation of the Hawaii paradigm and an alternative, plate-based hypothesis. *Earth-Sci. Rev.* **2025**, *261*, 105038. [CrossRef]
11. Iyer, S.D.; Mehta, C.M.; Das, P.; Kalangutkar, N.G. Seamounts—Characteristics, formation, mineral deposits and biodiversity. *Geol. Acta* **2012**, *10*, 295–308. [CrossRef]
12. Conrad, C.P.; Selway, K.; Hirschmann, M.M.; Ballmer, M.D.; Wessel, P. Constraints on volumes and patterns of asthenospheric melt from the space-time distribution of seamounts. *Geophys. Res. Lett.* **2017**, *44*, 7203–7210. [CrossRef]
13. Kim, S.S.; Wessel, P. New global seamount census from altimetry-derived gravity data. *Geophys. J. Int.* **2011**, *186*, 615–631. [CrossRef]
14. Harris, P.T.; Macmillan-Lawler, M.; Ruppc, J.; Baker, E.K. Geomorphology of the oceans. *Mar. Geol.* **2014**, *352*, 4–24. [CrossRef]
15. Wessel, P. Global distribution of seamounts inferred fromgridded Geosat/ERS-1 altimetry. *J. Geophys. Res.* **2001**, *106*, 19431–19441. [CrossRef]
16. Kitchingman, A.; Lai, S. Inferences on potential seamount locations from midresolution bathymetric data. In *FCRR Seamounts: Biodiversity and Fisheries*; Morato, T., Pauly, D., Eds.; Fisheries Centre Research Reports; University of British Columbia: Vancouver, BC, Canada, 2004; pp. 7–12.

17. Yesson, C.; Clark, M.R.; Taylor, M.L.; Rogers, A.D. The global distribution of seamounts based on 30 arc seconds bathymetry data. Deep Sea Research Part I: Oceanographic. *Res. Pap.* **2011**, *58*, 442–453.
18. Lonsdale, P.; Batiza, R. Hyaloclastite and lava flows on young seamounts examined with a submersible. *Geol. Soc. Am. Bull.* **1980**, *91*, 545–554. [CrossRef]
19. Batiza, R.; Fornari, D.J.; Vanko, D.A.; Lonsdale, P. Craters, calderas, and hyaloclastites on young Pacific seamounts. *J. Geophys. Res.* **1984**, *89*, 8371–8390. [CrossRef]
20. Fornari, D.J.; Ryan, W.B.F.; Fox, P.J. The Evolution of Craters and Calderas on Young Seamounts–Insights from Sea Marc-I and Sea Beam Sonar Surveys of a Small Seamount Group near the Axis of the East Pacific Rise at Approximately 10-Degrees-N. *J. Geophys. Res.* **1984**, *89*, 1069–1083. [CrossRef]
21. Vogt, P.R.; Smoot, N.C. The Geisha guyots—Multibeam bathymetry and morphometric interpretation. *J. Geophys. Res.* **1984**, *89*, 1085–1107. [CrossRef]
22. Moore, J.G.; Clague, D.A. Volcano growth and evolution of the island of Hawaii. *Geol. Soc. Am. Bull.* **1992**, *104*, 1471–1484. [CrossRef]
23. Wright, I.C.; Gamble, J.A. Southern Kermadec submarine caldera arc volcanoes (SW Pacific). Caldera formation by effusive and pyroclastic eruption. *Mar. Geol.* **1992**, *161*, 207–227. [CrossRef]
24. Clague, D.A.; Moore, J.G.; Andy Reynolds, J.R. Formation of submarine flat-topped volcanic cones in Hawaii. *Bull. Volcanol.* **2000**, *62*, 214–233. [CrossRef]
25. Mitchell, N.C. Transition from circular to stellate forms of submarine volcanoes. *J. Geophys. Res. Solid Earth* **2001**, *106*, 1987–2003. [CrossRef]
26. Mitchell, N.C.; Masson, D.G.; Watts, A.B.; Gee, M.J.R.; Urgeles, R. The morphology of the submarine flanks of volcanic ocean islands: A comparative study of the Canary and Hawaiian hotspot islands. *J. Volcanol. Geotherm. Res.* **2002**, *115*, 83–107. [CrossRef]
27. Mitchell, N.C. Susceptibility of mid-ocean ridge volcanic islands and seamounts to large-scale landsliding. *J. Geophys. Res.* **2003**, *108*, 2397. [CrossRef]
28. Chadwick, W.W.; Wright, I.C.; Schwarz-Schampera, U.; Hyvernaud, O.; Reymond, D.; de Ronde, C.E.J. Cyclic eruptions and sector collapses at Monowai submarine volcano, Kermadec arc: 1998–2007. *Geochem. Geophys. Geosyst.* **2008**, *9*, Q10014. [CrossRef]
29. Hoernle, K.; Hauff, F.; van den Bogaard, P.; Werner, R.; Mortimer, N.; Geldmacher, J.; Schönberg, D.G.; Davy, B. Age and geochemistry of volcanic rocks from the Hikurangi and Manihiki oceanic Plateaus. *Geochim. Cosmochim. Acta* **2010**, *74*, 7196–7219. [CrossRef]
30. Skolotnev, S.G.; Peyve, A.A.; Turko, N.N. New Data on the Structure of the Vitoria–Trindade Seamount Chain (Western Brazil Basin, South Atlantic). *Dokl. Earth Sci.* **2010**, *431*, 435–440. [CrossRef]
31. Skolotnev, S.G.; Peive, A.A.; Eskin, A.E. New Data on the Structure of the Bahia Seamounts (Western Portion of the Brazil Basin, South Atlantic). *Dokl. Earth Sci.* **2010**, *435*, 1581–1585. [CrossRef]
32. Dadd, K.A.; Locmelis, M.; Higgins, K.; Hashimoto, T. Cenozoic Volcanism of the Capel-Faust Basins, Lord Howe Rise, SW Pacific Ocean. *Deep-Sea Res. II* **2011**, *58*, 922–932. [CrossRef]
33. Zhang, T.; Lin, J.; Gao, J.Y. Interactions between hotspots and the Southwest Indian Ridge during the last 90 Ma: Implications on the formation of oceanic plateaus and intra-plate seamounts. *Sci. China Earth Sci.* **2011**, *54*, 1177–1188. [CrossRef]
34. Skolotnev, S.G.; Petrova, V.V.; Peyve, A.A. Origin of Submarine Volcanism at the Eastern Margin of the Central Atlantic: Investigation of the Alkaline Volcanic Rocks of the Carter Seamount (Grimaldi Seamounts). *Petrology* **2012**, *20*, 59–85. [CrossRef]
35. Milano, G.; Passaro, S.; Sprovieri, M. Present-day knowledge on the Palinuro Seamount (south-eastern Tyrrhenian Sea). *Boll. Di Geofis. Teor. Ed Appl.* **2012**, *53*, 403–416. [CrossRef]
36. Pe-Piper, G.; Meredyk, S.; Zhang, Y.; Piper, D.J.W.; Edinger, E. Petrology and tectonic significance of seamounts within transitional crust east of Orphan Knoll, offshore eastern Canada. *Geo-Marire Lett.* **2013**, *33*, 433–447. [CrossRef]
37. Anokhina, V.M.; Mel'nikovb, M.E. Morphostructural Features of the Butakov Guyot (Magellan Seamounts, Pacific Ocean). *Russ. J. Pac. Geol.* **2013**, *7*, 65–76. [CrossRef]
38. Tempera, F.; Hipólito, A.; Madeira, J.; Vieira, S.; Campos, A.S.; Mitchell, N.C. Condor seamount (Azores, NE Atlantic): A morpho-tectonic interpretation. *Deep-Sea Res. II* **2013**, *98*, 7–23. [CrossRef]
39. Leat, P.T.; Day, S.J.; Tate, A.J.; Martina, T.J.; Owene, M.J.; Tappin, D.R. Volcanic evolution of the South Sandwich volcanic arc, South Atlantic, from multibeam bathymetry. *J. Volcanol. Geotherm. Res.* **2013**, *265*, 60–77. [CrossRef]
40. Clague, D.A.; Dreyer, B.M.; Paduan, J.B.; Martin, J.F.; Chadwick, W.; Caress, D.W.; Portner, R.A.; Guilderson, T.P.; McGann, M.L.; Thomas, H.; et al. Geologic history of the summit of Axial Seamount, Juan de Fuca Ridge. *Geochem. Geophys. Geosyst.* **2013**, *14*, 4403–4443. [CrossRef]
41. Vanderkluysen, L.; Mahoney, J.J.; Koppers, A.A.P.; Beier, C.; Regelous, M.; Gee, J.S.; Lonsdale, P.F. Louisville Seamount Chain: Petrogenetic processes and geochemical evolution of the mantle source. *Geochem. Geophys. Geosyst.* **2014**, *15*, 2380–2400. [CrossRef]
42. Rodrigo, C.; Díaz, J.; González-Fernández, A. Origin of the Easter Submarine Alignment: Morphology and structural lineaments. *Lat. Am. J. Aquat. Res.* **2014**, *42*, 857–870. [CrossRef]

43. Varghese, S.; Nagendran, G. Morphometric analysis of Barren volcanic base and associated tectonic elements in the Andaman fore-arc sub-basin. *Curr. Sci.* **2015**, *108*, 694–698.
44. Mel'nikova, M.E.; Pletnevb, S.P.; Anokhinc, V.M.; Sedyshevaa, T.E.; Ivanova, V.V. Volcanic Edifices on Guyots of the Magellan Seamounts. *Russ. J. Pac. Geol.* **2016**, *10*, 435–442. [CrossRef]
45. Palomino, D.; Vázquez, J.T.; Somoza, L.; León, R.; López-González, N.; Medialdea, T.; Fernández-Salas, L.M.; González, F.J.; Rengel, J.A. Geomorphological features in the southern Canary Island Volcanic Province: The importance of volcanic processes and massive slope instabilities associated with seamounts. *Geomorphology* **2016**, *255*, 125–139. [CrossRef]
46. Rivera, J.; Canals, M.; Lastras, G.; Hermida, N.; Amblas, D.; Arrese, B.; Martín-Sosa, P.; Acosta, J. Morphometry of Concepcion Bank: Evidence of Geological and Biological Processes on a Large Volcanic Seamount of the Canary Islands Seamount Province. *PLoS ONE* **2016**, *11*, e0156337. [CrossRef]
47. Schnur, S.R.; Chadwick, W.; Embley, R.W.; Ferrini, V.L.; de Ronde, C.E.J.; Cashman, K.V.; Deardorff, N.D.; Merle, S.G.; Dziak, R.P.; Haxel, J.H.; et al. A decade of volcanic construction and destruction at the summit of NW Rota-1 seamount: 2004–2014. *J. Geophys. Res. Solid Earth* **2017**, *122*, 1558–1584. [CrossRef]
48. Moore, J.G.; Fiske, R.S. Volcanic substructure inferred from dredge samples and ocean-bottom photographs, Hawaii. *Geol. Soc. Am. Bull.* **1969**, *80*, 1191–1201. [CrossRef]
49. Fleet, A.J.; Mckelvey, B.C. Eocene explosive submarine volcanism, ninety east ridge, indian-ocean. *Mar. Geol.* **1978**, *26*, 73–97. [CrossRef]
50. Bryan, W.B.; Humphris, S.E.; Thompson, G.; Casey, J.F. Comparative volcanology of small axial eruptive centers in the MARK area. *J. Geophys. Res. Solid Earth* **1994**, *99*, 2973–2984. [CrossRef]
51. Walton, A.W.; Schiffman, P. Alteration of hyaloclastites in the HSDP 2 Phase 1 Drill Core—1. Description and paragénesis. *Geochem. Geophys. Geosyst.* **2003**, *4*, 8709. [CrossRef]
52. Schmincke, H.U.; Sumita, M. Chapter 54. Instability of Oceanic Volcanic Edifices: Examples of Sector Collapse, Debris Avalanches, and Debris Flows from Gran Canaria (Canary Islands). In *Submarine Mass Movements and Their Consequences 6th International Symposium*; Krastel, S., Behrmann, J.-H., Volker, D., Stipp, M., Berndt, C., Urgeles, R., Chaytor, J., Huhn, K., Strasser, M., Harbitz, C.B., Eds.; Advances in Natural and Technological Hazards Research; Springer International Publishing: Cham, Switzerland, 2014; Volume 37, pp. 605–616.
53. Tarduno, J.A.; Duncan, R.A.; Scholl, D.W.; Cottrell, R.D.; Steinberger, B.; Thordarson, T.; Kerr, B.C.; Neal, C.R.; Frey, F.A.; Torii, M.; et al. The Emperor Seamounts: Southward motion of the Hawaiian hotspot plume in earth's mantle. *Science* **2003**, *301*, 1064–1069. [CrossRef]
54. Clague, D.A.; Paduan, J.B.; Davis, A.S. Widespread strombolian eruptions of mid-ocean ridge basalt. *J. Volcanol. Geotherm. Res.* **2009**, *180*, 171–188. [CrossRef]
55. Clague, D.A.; Rubin, K.H.; Keller, N.S. Products of submarine fountains and bubble-burst activity at 1200 m on West Mata Volcano, Lau Basin. *EOS Trans. AGU* **2009**, *90*, V43I-02.
56. Koppers, A.A.P.; Russell, J.A.; Roberts, J.; Jackson, M.G.; Konter, J.G.; Wright, D.J.; Staudigel, H.; Hart, S.R. Age systematics of two young en echelon Samoan volcanic trails. *Geochem. Geophys. Geosyst.* **2011**, *12*, Q07025. [CrossRef]
57. Peyve, A.A. Seamounts in the East of South Atlantic: Origin and Correlation with Mesozoic–Cenozoic Magmatic Structures of West Africa. *Geotectonics* **2011**, *45*, 195–209. [CrossRef]
58. Shimoda, G.; Ishizuka, O.; Yamashita, K.; Yoshitake, M.; Ogasawara, M.; Yuasa, M. Tectonic influence on chemical composition of ocean island basalts in the West and South Pacific: Implication for a deep mantle origin. *Geochem. Geophys. Geosyst.* **2011**, *12*, Q07020. [CrossRef]
59. Barker, A.K.; Troll, V.R.; Ellam, M.R.; Hansteen, T.H.; Harris, C.; Stillman, C.J.; Andersson, A. Magmatic evolution of the Cadamosto Seamount, Cape Verde: Beyond the spatial extent of EM1. *Contrib. Mineral. Pet.* **2012**, *163*, 949–965. [CrossRef]
60. Skolotnev, S.G.; Peyvea, A.A.; Ivanovab, E.V.; Murdmaab, I.O.; Levchenkob, O.V.; Dmitrenkob, O.B. First Data about the Geochemistry and Geological Structure of Underwater Seamounts between Ascension and Bode Verde Transform Fracture Zones in the Brazilian Basin (South Atlantic). *Dokl. Earth Sci.* **2012**, *442*, 56–62. [CrossRef]
61. Koppers, A.A.P.; Yamazaki, T.; Geldmacher, J.; The IODP Expedition 330 Scientific Party. IODP Expedition 330: Drilling the Louisville Seamount Trail in the SW Pacific. Science Reports. *Sci. Drill.* **2013**, *15*, 11–22. [CrossRef]
62. Dreyer, B.M.; Clague, D.A.; Gill, J.B. Petrological variability of recent magmatism at the Axial Seamount Summit, Juan de Fuca Ridge. *Geochem. Geophys. Geosyst.* **2013**, *14*, 4306–4333. [CrossRef]
63. Lezzi, J.L.; Caso, C.; Ventura, G.; Vallefuoco, M.; Cavallo, A.; Behrens, H.; Mollo, S.; Paltrinieri, D.; Signanini, P.; Vetere, F. First documented deep submarine explosive eruptions at the Marsili Seamount (Tyrrhenian Sea, Italy): A case of historical volcanism in the Mediterranean Sea. *Gondwana Res.* **2014**, *25*, 764–774. [CrossRef]
64. Nichols, A.R.L.; Beier, C.; Brandl, P.A.; Buchs, D.M.; Krumm, S.H. Geochemistry of volcanic glasses from the Louisville Seamount Trail (IODP Expedition 330): Implications for eruption environments and mantle melting. *Geochem. Geophys. Geosyst.* **2014**, *15*, 1718–1738. [CrossRef]

65. Skolotnev, S.G.; Peyve, A.A.; Bylinskaya, M.E.; Golovina, L.A. New Data on the Composition and Age of Rocks from the Bathymetrists Seamounts (Eastern Margin of the Equatorial Atlantic). *Dokl. Earth Sci.* **2017**, *472*, 20–25. [CrossRef]
66. Eisele, S.; Reißig, S.; Freundt, A.; Kutterolf, S.; Nürnberg, D.; Wang, K.; Kwasnitschka, T. Pleistocene to Holocene offshore tephrostratigraphy of highly explosive eruptions from the southwestern Cape Verde Archipelago. *Mar. Geol.* **2015**, *369*, 233–250. [CrossRef]
67. Yan, Q.; Castillo, P.; Shi, X.; Wang, L.; Liao, L.; Ren, J. Geochemistry and petrogenesis of volcanic rocks from Daimao Seamount (South China Sea) and their tectonic implications. *Lithos* **2015**, *218–219*, 117–126. [CrossRef]
68. Zhang, Y.; Meng, F.; Niu, Y. Hf isotope systematics of seamounts near the East Pacific Rise (EPR) and geodynamic implications. *Lithos* **2016**, *262*, 107–119. [CrossRef]
69. Buchs, D.M.; Williams, R.; Sano, S.; Wright, V.P. Non-Hawaiian lithostratigraphy of Louisville seamounts and the formation of high-latitude oceanic islands and guyots. *J. Volcanol. Geotherm. Res.* **2018**, *356*, 1–23. [CrossRef]
70. Hanyu, T.; Tejada, M.L.G.; Shimizub, K.; Ishizuka, O.; Fujii, T.; Kimura, J.; Changa, Q.; Senda, R.; Miyazaki, T.; Hirahara, Y.; et al. Collision-induced post-plateau volcanism: Evidence from a seamount on Ontong Java Plateau. *Lithos* **2017**, *294–295*, 87–96. [CrossRef]
71. Pinto Ribeiro, L.; Martins, S.; Hildenbrand, A.; Madureira, P.; Mata, J. The genetic link between the Azores Archipelago and the Southern Azores Seamount Chain (SASC): The elemental, isotopic and chronological evidences. *Lithos* **2017**, *294–295*, 133–146. [CrossRef]
72. Schiffman, P.; Watters, R.J.; Thompson, N.; Walton, W. Hyaloclastites and the slope stability of Hawaiian volcanoes: Insights from the Hawaiian Scientific Drilling Project's 3-km drill core. *J. Volcanol. Geotherm. Res.* **2006**, *151*, 217–228.
73. Quane, S.; Garcia, M.; Guillou, H.; Hulsebosch, T. Magmatic history of the East Rift Zone of Kilauea Volcano, Hawaii based on drill core from SOH 1. *J. Volcanol. Geotherm. Res.* **2000**, *102*, 319–338. [CrossRef]
74. Sánchez-Guzman, J.; Abad, J. El sondeo geotérmico Lanzarote-1. Significado geólogico y geotérmico. In *Anales de Física (Serie B). Número Especial*; Real Sociedad Española de Física: Madrid, Spain, 1986; Volume 82, pp. 102–109.
75. Fornari, D.J.; Peterson, D.W.; Lockwood, J.P.; Malahoff, A.; Heezen, B.C. Submarine extension of the southwest rift zone of Mauna Loa volcano, Hawaii: Visual observations from U.S. Navy deep submergence vehicle (DSV) Sea Cliff. *Geol. Soc. Am. Bull.* **1979**, *90*, 435–443. [CrossRef]
76. Fornari, D.J.; Malahoff, A.; Heezen, B.C. Submarine slope micromorphology and volcanic substructure of the island of Hawaii inferred from visual observa-tions made from U.S. Navy deep-submergence vehicle (DSV) Sea Cliff. *Mar. Geol.* **1979**, *32*, 1–20. [CrossRef]
77. Fornari, D.J.; Malahoff, A.; Heezen, B.C. Visual observations of the volcanic micromorphology of Tortuga, Lorraine and Tutu Seamounts; and petrology and chemistry of ridge and seamount features in and around the Panama Basin. *Mar. Geol.* **1979**, *31*, 1–30. [CrossRef]
78. Chadwick, W.W.; Cashman, K.V.; Embley, R.W.; Matsumoto, H.; Dziak, R.P.; de Ronde, C.E.J.; Lau, T.K.; Deardorff, N.D.; Merle, S.G. Direct video and hydrophone observations of submarine explosive eruptions at NW Rota-1 volcano, Mariana arc. *J. Geophys. Res.* **2008**, *113*, B08S10. [CrossRef]
79. Chadwick, W.W.; Embley, R.W.; Baker, E.T.; Resing, J.A.; Lupton, J.E.; Cashman, K.V.; Dziak, R.P.; Tunnicliffe, V.; Butterfield, D.A.; Tamura, Y. SPOTLIGHT 10 Northwest Rota-1 Seamount 14°36.048′ N, 144°46.519′ E. *Oceanography* **2010**, *23*, 182–183. [CrossRef]
80. Schipper, C.I.; White, J.D.L. No depth limit to hydrovolcanic limu o Pele: Analysis of limu from Lō'ihi Seamount, Hawai'i. *Bull. Volcanol.* **2010**, *72*, 149–164. [CrossRef]
81. Schipper, C.I.; White, J.D.L.; Houghton, B.F.; Shimizu, N.; Stewart, R.B. Explosive submarine eruptions driven by volatile-coupled degassing at Lō'ihi Seamount, Hawai'i. *Earth Planet. Sci. Lett.* **2010**, *295*, 497–510. [CrossRef]
82. Schipper, C.I.; White, J.D.; Houghton, B.F. Syn- and post-fragmentation textures in submarine pyroclasts from Lō'ihi Seamount, Hawai'i. *J. Volcanol. Geotherm. Res.* **2010**, *191*, 93–106. [CrossRef]
83. Schipper, C.I.; White, J.D.L.; Houghton, B.F. Textural, geochemical, and volatile evidence for a Strombolian-like eruption sequence at Lō'ihi Seamount, Hawai'i. *J. Volcanol. Geotherm. Res.* **2011**, *207*, 16–32. [CrossRef]
84. Chadwick, W.; Merle, S.G.; Buck, N.J.; Lavelle, W.; Resing, J.A.; Ferrini, V. Imaging of CO2 bubble plumes above an erupting submarine volcano, NW Rota-1, Mariana Arc. *Geochem. Geophys. Geosyst.* **2014**, *15*, 4325–4342. [CrossRef]
85. Portner, R.A.; Clague, D.A.; Paduan, J.B. Caldera formation and varied eruption styles on North Pacific seamounts: The clastic lithofacies record. *Bull. Volcanol.* **2014**, *76*, 845. [CrossRef]
86. Portner, R.A.; Clague, D.A.; Heloc, C.; Dreyer, B.M.; Paduan, J.B. Contrasting styles of deep-marine pyroclastic eruptions revealed from Axial Seamount push core records. *Earth Planet. Sci. Lett.* **2015**, *423*, 219–231. [CrossRef]
87. Embley, R.W.; Chadwick, W.W.; Baker, E.T.; Butterfield, D.A.; Resing, J.A.; De Ronde, C.E.J.; Tunnicliffe, V.; Lupton, J.E.; Juniper, S.K.; Rubin, K.H.; et al. Long-term eruptive activity at a submarine arc volcano. *Nature* **2006**, *441*, 494–497. [CrossRef]
88. Konter, J.G.; Staudigel, H.; Blichert-Toft, J.; Hanan, B.B.; Polvé, J.R.; Davies, M.; Shimizu, N.; Schiffman, P. Geochemical stages at Jasper Seamount and the origin of intraplate volcanoes. *Geochem. Geophys. Geosyst.* **2009**, *10*, Q02001. [CrossRef]

89. Davis, A.S.; Clague, D.A.; Paduan, J.B.; Cousens, B.L.; Huard, J. Origin of volcanic seamounts at the continental margin of California related to changes in plate margins. *Geochem. Geophys. Geosyst.* **2010**, *11*, Q05006. [CrossRef]
90. Deardorff, N.D.; Cashman, K.V.; Chadwick, W.W. Observations of eruptive plume dynamics and pyroclastic deposits from submarineexplosive eruptions at NW Rota-1, Mariana arc. *J. Volcanol. Geotherm. Res.* **2011**, *202*, 47–59. [CrossRef]
91. Coumans, J.P.; Stix, J.; Clague, D.A.; Minarik, W.G. The Magmatic Architecture of Taney Seamount-A, NE Pacific Ocean. *J. Petrol.* **2015**, *56*, 1037–1067. [CrossRef]
92. Schwartz, D.M.; Wanless, V.D.; Berg, R.; Jones, M.P.; Fornari, D.J.; Soule, S.A.; Lytle, M.L.; Carey, S. Petrogenesis of alkalic seamounts on the Galápagos Platform. *Deep. Sea Res. Part II Top. Stud. Oceanogr.* **2018**, *150*, 170–180. [CrossRef]
93. Kelley, D.S.; Delaney, J.R.; Juniper, S.K. Establishing a new era of submarine volcanic observatories: Cabling Axial Seamount and the Endeavour Segment of the Juan de Fuca Ridge. *Mar. Geol.* **2014**, *352*, 426–450. [CrossRef]
94. Nooner, S.L.; Chadwick, W.W. Inflation-predictable behavior and co-eruption deformation at Axial Seamount. *Science* **2016**, *354*, 1399–1403. [CrossRef]
95. Sigmundsson, F. New insights into magma plumbing along rift systems from detailed observations of eruptive behavior at Axial volcano. *Geophys. Res. Lett.* **2016**, *43*, 12423–12427. [CrossRef]
96. Wilcock, W.S.D.; Dziak, R.P.; Tolstoy, M.; Chadwick, W.W., Jr.; Nooner, S.L.; Bohnenstiehl, D.R.; Caplan-Auerbach, J.; Waldhauser, F.; Arnulf, A.F.; Baillard, C.; et al. The recent volcanic history of Axial Seamount: Geophysical insights into past eruption dynamics with an eye toward enhanced observations of future eruptions. *Oceanography* **2018**, *31*, 114–123. [CrossRef]
97. Tolstoy, M.; Wilcock, M.S.D.; Tan, Y.J.; Waldhauser, F. A tale of two eruptions: How data from Axial Seamount led to a discovery on the East Pacific Rise. *Oceanography* **2018**, *31*, 124–125. [CrossRef]
98. Hildebrand, J.A.; Dorman, L.M.; Hammer, P.T.C.; Schreiner, A.E.; Cornuelle, B.D. Seismic tomography of Jasper Seamount. *Geophys. Res. Lett.* **1989**, *16*, 1355–1358. [CrossRef]
99. Hildebrand, J.A.; Stevenson, J.M.; Hammer, P.T.C.; Zumberge, M.A.; Parker, R.L.; Fox, C.G.; Meis, P.J. A seafloor and sea surface gravity survey of Axial Volcano. *J. Geophys. Res. Solid Earth* **1990**, *95*, 12751–12763. [CrossRef]
100. Hammer, P.T.C.; Dorman, L.M.; Hildebrand, J.A.; Cornuelle, B.D. Jasper Seamount structure: Seafloor seismic refraction tomography. *J. Geophys. Res. Solid Earth* **1994**, *99*, 6731–6752. [CrossRef]
101. Gilbert, L.A.; McDuff, R.E.; Johnson, H.P. Porosity of the upper edifice of Axial Seamount. *Geology* **2007**, *35*, 49–52. [CrossRef]
102. García-Abdeslem, J. Density modeling of the Escollos Alijos Seamount from inversion of its geoid undulation anomaly. *Geofísica Int.* **2014**, *53*, 333–341. [CrossRef]
103. Lomtev, V.L.; Patrikeev, V.N. New Evidence for the Structure of Conical Seamounts and Hills at the Foot of the Sea of Okhotsk Margin of the Kuril Island Arc: Continuous SeismicProfiling Data. *J. Volcanol. Seismol.* **2015**, *9*, 104–115. [CrossRef]
104. Wang, J.; Zhao, M.; Qiu, X.; Sibuet, J.C.; He, E.; Zhang, J.; Tao, C. 3D seismic structure of the Zhenbei–Huangyan seamounts chain in the East Sub-basin of the South China Sea and its mechanism of formation. *Geol. J.* **2016**, *51*, 448–463. [CrossRef]
105. Jokat, W.; Reents, S. Hotspot volcanism in the southern South Atlantic: Geophysical constraints on the evolution of the southernWalvis Ridge and the Discovery Seamounts. *Tectonophysics* **2017**, *716*, 77–89. [CrossRef]
106. Jones, J.G. Intraglacial volcanoes of south-west iceland and their significance in interpretation of form of marine basaltic volcanoes. *Nature* **1966**, *212*, 586–588. [CrossRef]
107. Macpherson, G.J. The Snow Mountain volcanic complex—An on-land seamount in the franciscan terrain, California. *J. Geol.* **1983**, *91*, 73–92. [CrossRef]
108. Staudigel, H.; Schmincke, H.U. The pliocene seamount series of La Palma Canary-Islands. *J. Geophys. Res.* **1984**, *89*, 1195–1215. [CrossRef]
109. Staudigel, H.; Feraud, G.; Giannerini, G. The history of intrusive activity on the Island of La Palma (Canary Islands). *J. Volcanol. Geotherm. Res.* **1986**, *2*, 299–322. [CrossRef]
110. Ayres, L.D.; Van Wagoner, N.A.; Ferreira, W.S. Voluminous shallow-water to emergent phreatomagmatic basaltic volcaniclastic rocks, Proterozoic (−1886 Ma) Amisk Lake composite volcano, Fhn Flon Greenstone Belt, Canada. *SEPM Spec. Publ.* **1991**, *45*, 175–187.
111. Kano, K.; Yamamoto, T.; Takeuchi, K. A miocene island-arc volcanic seamount—The Takashibiyama formation, Shimane peninsula, sw Japan. *J. Volcanol. Geotherm. Res.* **1993**, *59*, 101–119. [CrossRef]
112. Mcphie, J. A pliocene shoaling basaltic seamount: Ba volcanic group at Rakiraki, Fiji. *J. Volcanol. Geotherm. Res.* **1995**, *64*, 193–210. [CrossRef]
113. Meyer, J.; Mercolli, I.; Immenhauser, A. Off-ridge alkaline magmatism and seamount volcanoes in the Masirah island ophiolite, Oman. *Tectonophysics* **1996**, *267*, 187–208. [CrossRef]
114. Corcoran, P.L. Recognizing distinct portions of seamounts using volcanic facies analysis: Examples from the Archean Slave Province, NWT, Canada. *Precambrian Res.* **2000**, *101*, 237–261. [CrossRef]

115. Gutiérrez, M. Estudio Petrológico, Geoquímico y Estructural de la Serie Volcánica Submarina del Complejo Basal de Fuerteventura (Islas Canarias): Caracterización del Crecimiento Submarino y de la Emersión de la Isla. Ph.D. Thesis, Department of Pedology and Geology, Universidad de La Laguna, La Laguna, Spain, 2000; pp. 1–533.
116. Gutiérrez, M.; Casillas, R.; Fernández, C.; Balogh, K.; Ahijado, A.; Castillo, C. La serie volcánica submarina del Complejo Basal de Fuerteventura: Crecimiento submarino y emersión de la isla. *Geogaceta* **2002**, *32*, 250–254.
117. Gutiérrez, M.; Casillas, R.; Fernández, C.; Balogh, K.; Ahijado, A.; Castillo, C.; Colmenero, J.R.; García-Navarro, E. The submarine volcanic succession of the Basal Complex of Fuerteventura, Canary Islands: A model of submarine growth and emersion of some tectonic volcanic islands. *Geol. Soc. Am. Bull.* **2006**, *118*, 785–804. [CrossRef]
118. Buchs, D.M.; Arculus, R.J.; Baumgartner, P.O.; Ulianov, A. Oceanic intraplate volcanoes exposed: Example from seamounts accreted in Panama. *Geology* **2011**, *39*, 335–338. [CrossRef]
119. Schnur, S.R.; Gilbert, L.A. Detailed volcanostratigraphy of an accreted seamount: Implications for intraplate seamount formation. *Geochem. Geophys. Geosyst.* **2012**, *13*, Q0AM05. [CrossRef]
120. Suiting, I.; Schmincke, H.U. Iblean diatremes 3: Volcanic processes on aMiocene carbonate platform (Iblean Mountains, SE-Sicily): A comparison of deep vs. shallow marine eruptive processes. *Bull. Volcanol.* **2012**, *74*, 207–230. [CrossRef]
121. Safonova, I.; Maruyama, S.; Kojima, S.; Komiya, T.; Krivonogov, S.; Koshida, K. Recognizing OIB and MORB in accretionary complexes: A new approach based on ocean plate stratigraphy, petrology and geochemistry. *Gondwana Res.* **2016**, *33*, 92–114. [CrossRef]
122. Staudigel, H.; Clague, D.A. The Geological History of Deep-Sea Volcanoes Biosphere, Hydrosphere, and Lithosphere Interactions. *Oceanography* **2010**, *23*, 58–71. [CrossRef]
123. Fúster, J.M.; Cendrero, A.; Gastesi, P.; Ibarrola, E.; López Ruiz, J. *Geología y Volcanología de las Islas Canarias—Fuerteventura*; Instituto 'Lucas Mallada': Huesca, Spain; Consejo Superior de Investigaciones Científicas: Madrid, Spain, 1968; pp. 1–239.
124. Cendrero, A. Estudio Geológico y Petrológico del complejo basal de la Isla de La Gomera (Canarias). *Estud. Geológicos* **1971**, *27*, 3–73.
125. Stillman, C.J.; Fúster, J.M.; Bennell-Baker, M.J.; Muñoz, M.; Smewing, J.D.; Sagredo, J. Basal Complex of Fuerteventura (Canary Islands) is an oceanic intrusive complex with rift-system affinities. *Nature* **1975**, *257*, 469–471. [CrossRef]
126. Cendrero, A. Nota previa sobre la geologia del Complejo Basal de la isla de La Gomera (Canarias). *Estud. Geológicos* **1967**, *23*, 71–79.
127. Cendrero, A. The Volcano-plutonic Complex of La Gomera. *Bull. Volcanol.* **1970**, *84*, 561–587.
128. Hernández-Pacheco, A. Nota previa sobre el Complejo Basal de la Isla de La Palma (Canarias). *Estud. Geológicos* **1971**, *27*, 255–265.
129. Henández-Pacheco, A.; y Fernández-Santín, S. Las formaciones volcánicas submarinas de la Caldera de Taburiente en La Palma (Canarias) y sus transformaciones metasomaticas. In Proceedings of the Symposium on Andean and Antarctic Volcanology Problems; IAVCEI: Santiago, Chile, 1974; p. 14.
130. Muñoz, M.; Sagredo, J. Existencia de metamorfismos superpuestos en el Complejo Basal de Fuerteventura (Canarias). In Proceedings of the I Asamblea Nacional de Geodesia y Geofísica, Madrid, Spain, 16–19 December 1974; pp. 1287–1288.
131. Robertson, A.H.F.; Stillman, C.J. Late Mesozoic sedimentary rocks of Fuerteventura, Canary Islands. Implications for West Africa continental margin evolution. *J. Geol. Soc. Lond.* **1979**, *136*, 47–60.
132. Robertson, A.H.F.; Stillman, C.J. Submarine volcanic and associated sedimentary rocks of the Fuerteventura Basal Complex, Canary Islands. *Geol. Mag.* **1979**, *116*, 203–214. [CrossRef]
133. Fúster, J.M.; Muñoz, M.; Sagredo, J.; Yébenes, A.; Bravo, T.; Hernández-Pacheco, A. Excursión n° 121 A + c del 26° I.G.C. a las Islas Canarias. *Boletín Inst. Geológico Min. España* **1980**, *92*, 351–390.
134. Robertson, A.H.F.; Bernouilli, D. Stratigraphy facies significance of Late Mesozoic Early Tertiary sedimentary rocks of Fuerteventura (Canary Islands), Maio (Cape Verde Islands). In *Geology of the Northwest African Continental Margin*; Von Rad, U., Hinz, K., Sarnthein, M., y Seibold, E., Eds.; Springer: Berlin/Heidelberg, Germany, 1982; pp. 498–525.
135. Cantagrel, J.M.; Fúster, J.M.; Pin, C.; Renaud, U.; Ibarrola, E. Age Miocène inférieur des carbonatites de Fuerteventura. *C. R. Acad. Sci. Paris* **1993**, *316*, 1147–1153.
136. De la Nuez, J. El Complejo Intrusivo Subvolcánico de la Caldera de Taburiente (La Palma, Canarias). Ph.D. Thesis, Universidad Complutense de Madrid, Madrid, Spain, 1984; p. 401.
137. Le Bas, M.J.; Rex, D.C.; Stillman, C.J. The early magmatic chronology of Fuerteventura, Canary Islands. *Geol. Mag.* **1986**, *123*, 287–298. [CrossRef]
138. Stillman, C.J. A Canary Islands Dyke Swarm: Implications for the formation of oceanic islands by extensional fissural volcanism. In *Mafic Dyke Swarms*; Special Paper 34; Halls, H.C., Fahrig, W.J., Eds.; Geological Association of Canada: Toronto, ON, Canada, 1987; pp. 243–255.
139. Muñoz, M.; Sagredo, J. Características del metamorfismo térmico producido por los eventos plutónicos intrusivos más recientes del Complejo Basal de Fuerteventura. In Proceedings of the ESF Meeting on Canarian Volcanism, Lanzarote, Spain, 30 November–3 December 1989; pp. 104–108.

140. Sagredo, J.; Ancochea, E.; Brändle, J.L.; Cubas, C.R.; Fúster, J.M.; Hernandez-Pacheco, A.; y Muñoz, M. Magmatismo hipoabisal-subvolcánico y vulcanismo en un ámbito geodinámico distensivo (Fuerteventura, Islas Canarias). In Proceedings of the Meeting on Canarian Volcanism, Lanzarote, Spain, 30 November–3 December 1989.
141. Ahijado, A.; Hernández-Pacheco, A. Las rocas ultramáficas alcalinas del Jable de Salinas, Fuerteventura, Islas Canarias. *Rev. Soc. Geológica España* **1990**, *3*, 275–287.
142. Ahijado, A.; Palacios, T. Synchysita en las carbonatitas de la Pta. del Peñón Blanco, Fuerteventura, Islas Canarias. *Geogaceta* **1991**, *10*, 83–84.
143. Ahijado, A.; Hernández-Pacheco, A.; Mata, J. Características geoquímicas de las carbonatitas de la Punta del Peñon Blanco. Fuerteventura. Canarias. *Geogaceta* **1991**, *11*, 120–122.
144. Ahijado, A. Características mineralógicas de una sövita pirofanítica de la Pta. del Peñón Blanco, Fuerteventura, Canarias. *Geogaceta* **1992**, *12*, 81–82.
145. Ahijado, A.; y Hernández-Pacheco, A. El complejo ultramáfico-carbonatítico del Macizo de Amanay, Fuerteventura, Islas Canarias. *Actas III Congr. Geológico España VIII Congr. Latinoam. Geol.* **1992**, *1*, 315–318.
146. Renz, O.; Bernoulli, D.; Hottinger, L. Cretaceous ammonites from Fuerteventura, Canary Islands. *Geol. Mag.* **1992**, *129*, 763–769. [CrossRef]
147. Muñoz, M.; Sagredo, J. Reajustes mineralógicos y geoquímicos producidos durante el metamorfismo de contacto de diques basálticos (Fuerteventura, Islas Canarias). *Boletín Soc. Española Mineral.* **1994**, *17*, 86–87.
148. Ancochea, E.; Brandle, J.L.; Cubas, C.R.; Hernán, F.; Huertas, M.J. Volcanic complexes in the eastern ridge of the Canary Islands: The Miocene activity of the Island of Fuerteventura. *J. Volcanol. Geotherm. Res.* **1996**, *70*, 183–204. [CrossRef]
149. Hobson, A.; Bussy, F.; Hernández, J. Shallow-level migmatization of gabbros in a metamorphic contact aureole, Fuerteventura Basal Complex, Canary Islands. *J. Petrol.* **1998**, *39*, 125–137. [CrossRef]
150. Steiner, C.; Hobson, A.; Favre, P.; Stampli, G.M. Early Jurassic sea-floor spreading in the central Atlantic—The Jurassic sequence of Fuerteventura (Canary Islands). *Geol. Soc. Am. Bull.* **1998**, *110*, 1304–1317. [CrossRef]
151. Ahijado, A. Las Intrusiones Plutónicas e Hipoabisales del Sector Meridional del Complejo Basal de Fuerteventura. Ph.D. Thesis, Universidad Complutense de Madrid, Madrid, Spain, 1999; pp. 1–386.
152. Balogh, K.; Ahijado, A.; Casillas, R.; Fernández, C. Contributions to the chronology of the Basal Complex of Fuerteventura, Canary Islands. *J. Volcanol. Geotherm. Res.* **1999**, *90*, 81–102. [CrossRef]
153. Ahijado, A.; Casillas, R.; Hernandez-Pacheco, A. The dike swarms of the Amanay Massif, Fuerteventura, Canary Islands. *J. Asian Earth Sci.* **2001**, *19*, 333–345. [CrossRef]
154. Carracedo, J.C.; Badiola, E.R.; Guillou, H.; De La Nuez, J.; Pérez Torrado, F.J. Geology and volcanology of La Palma and El Hierro, Western Canaries. *Estud. Geol.* **2001**, *57*, 175–273. [CrossRef]
155. Demény, A.; Vennemann, T.W.; Hegner, E.; Ahijado, A.; Casillas, R.; Nagy, G.; Homonnay, Z.; Gutierrez, M.; Szabo, C. H, O, Sr, Nd, and Pb isotopic evidence for recycled oceanic crust in the Transitional Volcanic Group of Fuerteventura, Canary Islands, Spain. *Chem. Geol.* **2004**, *205*, 37–54. [CrossRef]
156. Ahijado, A.; Casillas, R.; Nagy, G.; Fernández, C. Sr-rich minerals in a carbonatite skarn, Fuerteventura, Canary Islands (Spain). *Mineral. Petrol.* **2005**, *84*, 107–127. [CrossRef]
157. Muñoz, M.; Sagredo, J.; De Ignacio, C.; Fernández-Santín, S.; Jeffries, T.E. New data (U-Pb, K-Ar) on the geochronology of the alkaline-carbonatitic association of Fuerteventura, Canary Islands, Spain. *Lithos* **2005**, *85*, 140–153. [CrossRef]
158. Fernández, C.; Casillas, R.; García-Navarro, E.; Gutiérrez, M.; Camacho, M.; Ahijado, A. Miocene rifting of Fuerteventura (Canary Islands). *Tectonics* **2006**, *21*, 13-1–13-18. [CrossRef]
159. Casillas, R.; de la Nuez, J.; Fernández, C.; García-Navarro, E.; Colmenero, J.R.; Martín, M.C. La secuencia volcánica submarina del Complejo Basal de La Gomera. *Geotemas* **2008**, *10*, 1273–1276.
160. Casillas, R.; Fernández, C.; Ahijado, A.; Gutiérrez, M.; García-Navarro, E.; Camacho, M. Excursión post-congreso n° 2: Crecimiento temprano y evolución tectónica de la Isla de Fuerteventura. In *Geoguía n° 6: Itinerarios Geológicos por las Islas Canarias: Fuerteventura, Lanzarote, La Gomera y El Hierro*; Pérez-Torrado, F., Cabrera, M.C., Eds.; Sociedad Geológica de España: Salamanca, Spain, 2008; pp. 59–89.
161. Casillas, R.C.; Fernández, C.; Colmenero, J.R. Crecimiento temprano y evolución geológica de la Isla de Fuerteventura. In Proceedings of the 8ª Reunión del Grupo Ibérico de Petrología, Geoquímica y Geocronología, Fuerteventura, Spain, 14–17 June 2023; Comisión de Petrología, Geoquímica y Geocronología de Rocas Ígneas y Metamórficas de la Sociedad Geológica de España: La Laguna, Spain, 2023; pp. 1–191.
162. Demény, A.; Casillas, R.; Vennemann, T.W.; Hegner, E.; Nagy, G.; Ahijado, A.; De La Nuez, J.; Sipos, P.; Pilet, S.; Milton, J. *Plume-Related Stable Isotope Compositions and Fluid–Rock Interaction Processes in the Basal Complex of La Palma, Canary Islands*; Spain Geological Society: London, UK, 2008; Volume 293, pp. 155–175.
163. Démeny, A.; Casillas, R.; de la Nuez, J.; Milton, J.A.; Nagy, G. Carbonate xenoliths in La Palma: Carbonatite or alteration product? *Chem. Der Erde Geochem.* **2008**, *68*, 369–381. [CrossRef]

164. Herrera, R.; Huertas, M.J.; Ancochea, E. Edades ^{40}Ar-^{39}Ar del Complejo Basal de la isla de La Gomera. *Geogaceta* **2008**, *44*, 7–10.
165. Holloway, M.; Bussy, F. Trace element distribution among rock-forming minerals from metamorphosed to partially molten basic igneous rocks in a contact aureole (Fuerteventura, Canaries). *Lithos* **2008**, *102*, 616–639. [CrossRef]
166. Holloway, M.I.; Bussy, F.; Vennemann, T.W. Low-pressure, water-assisted anatexis of basic dykes in a contact metamorphic aureole, Fuerteventura (Canary Islands): Oxygen isotope evidence for a meteoric fluid origin. *Contrib. Mineral. Petrol.* **2007**, *155*, 111–121. [CrossRef]
167. Casillas, R.; Fernández, C.; Colmenero, J.R.; Nuez, J.; García-Navarro, E.; Martín, C. Deformation structures associated with the Tazo landslide (La Gomera, Canary Islands). *Bull. Volcanol.* **2010**, *72*, 945–960. [CrossRef]
168. Démeny, A.; Casillas, R.; Hegner, E.; Vennemann, T.W.; Nagy, G.; Sipos, P. Geochemical and H-O-Sr-Nd isotope evidence for magmatic processes and meteoric-water interactions in the Basal Complex of La Gomera, Canary Islands. *Mineral. Petrol.* **2010**, *98*, 181–195. [CrossRef]
169. Allibon, J.; Bussy, F.; Lewin, E.; Darbellay, B. The tectonically controlled emplacement of a vertically sheeted gabbro–pyroxenite intrusion: Feeder-zone of an ocean-island volcano (Fuerteventura, Canary Islands). *Tectonophysics* **2011**, *500*, 78–97.
170. Allibon, J.; Ovtcharova, M.; Bussy, F.; Cosca, M.; Schaltegger, U.; Bussien, D.; Lewin, E. Lifetime of an ocean island volcano feeder zone: Constraints from U–Pb dating on coexisting zircon and baddeleyite, and ^{40}Ar/^{39}Ar age determinations, Fuerteventura, Canary Islands. *Can. J. Earth Sci.* **2011**, *48*, 567–592. [CrossRef]
171. Casillas, R.; Démeny, A.; Nagy, G.; Ahijado, A.; Fernández, C. Metacarbonatites in the Basal Complex of Fuerteventura (Canary Islands). The role of fluid/rock interactions during contact metamorphism and anatexis. *Lithos* **2011**, *125*, 503–520. [CrossRef]
172. Fernández, C.; Casillas, R.; de la Nuez, J.; Garcia-Navarro, E.; Camacho, M.A. Deformation of the substratum of a large shield volcano: Triggering factor for fast flank collapses in the old volcanic edifice of La Gomera, Canary Islands. *Geol. Soc. Am. Bull.* **2014**, *127*, 443–463. [CrossRef]
173. De la Nuez, J.; Casillas, R.; Quesada, M.L.; Fernández, C.; Colmenero, J.R. Caracterización geoquímica del complejo lóbulo-hialoclastítico submarino de la Caldera de Taburiente (La Palma, Islas Canarias). *Geotemas* **2016**, *16*, 407–411.
174. Casillas, R.; de la Nuez, J.; Colmenero, J.R.; Fernández, C. El Complejo Lóbulo-Hialoclastítico Traquítico de la Caldera de Taburiente (La Palma, Islas Canarias). *Geotemas* **2016**, *16*, 399–403.
175. Tornare, E.; Pilet, S.; Bussy, F. Magma Differentiation in Vertical conduits Revealed by the Complementary Study of Plutonic and Volcanic Rocks from Fuerteventura (Canary Islands). *J. Petrol.* **2016**, *57*, 2221–2250. [CrossRef]
176. Dahobeitia, J.J.; Banda, E. Geophysical setting of the Canary Archipielago. In Proceedings of the ESF Meeting on Canarian Volcanism, Lanzarote, Canary Islands, Spain, 30 November–3 December 1989; pp. 72–76.
177. Klitgord, K.; Schouten, H. Plate kinematics of the Central Atlantic. In *The Western North Atlantic Region*; Geological Society of America: Boulder, CO, USA, 1986. [CrossRef]
178. Prieto, G.A.; Parker, R.L.; Vernon, F.L. A Fortran 90 library for multitaper spectrum analysis. *Comput. Geosci.* **2009**, *35*, 1701–1710. [CrossRef]
179. Di Paolo, F.; Ledo, J.; Ślęzak, K.; van Dorth, D.M.; Cabrera-Pérez, I.; Pérez, N.M. La Palma island (Spain) geothermal system revealed by 3D magnetotelluric data inversion. *Sci. Rep.* **2020**, *10*, 18181. [CrossRef]
180. D'aUria, L.; Koulakov, I.; Prudencio, J.; Cabrera-Pérez, I.; Ibáñez, J.M.; Barrancos, J.; García-Hernández, R.; van Dorth, D.M.; Padilla, G.D.; Przeor, M.; et al. Rapid magma ascent beneath La Palma revealed by seismic tomography. *Sci. Rep.* **2022**, *12*, 17654. [CrossRef]
181. Casillas, R.; De la Nuez, J.; Fernández, C.; Colmenero, J.R.; Harangi, S.; Lukács, R.; Jourdan, F. Edad de las rocas volcánicas submarinas y plutónicas del Complejo Basal de La Palma: Implicaciones en la evolución geológica temprana de la Isla. *Geogaceta* **2020**, *67*, 47–50.
182. Arenas Martín, R.; Nuez Pestana, J.D.L. Características del metamorfismo hidrotermal del Complejo ·Plutónico de la Caldera de Taburiente (La Palma, Canarias). *Geogaceta* **1987**, *3*, 13–15.
183. Schiffman, P.; Staudigel, H. The smectite to chlorite transition in a fossil seamount hydrothermal system: The Basement Complex of La Palma, Canary Islands. *J. Metamorph. Geol.* **1995**, *13*, 487–498. [CrossRef]
184. Castillo, C.; Usera, J.; Liché, D.; De la Nuez, J.; Casillas, R. Estudio preliminar de los foraminíferos de la formación volcánica submarina de La Palma (Islas Canarias). In Proceedings of the XVIII Jornadas de la Sociedad Española de Paleontología-II Congreso Ibérico de Paleontología, Salamanca, Spain, 24 September–29 September 2002; pp. 29–30.
185. Coello, J. Las aguas subterráneas en las formaciones volcánicas del Norte de La Palma (Islas Canarias). In Proceedings of the Simposio Internacional de Recursos Hidráulicos: Canarias Agua 2000, Canarias, Spain, April 1987; pp. 1–19.
186. Ancochea, E.; Hernán, F.; Cendrero, A.; Cantagrel, J.M.; Fúster, J.M.; Ibarrola, E.; Coello, J. Constructive and destructive episodes in the building of a young oceanic island, La Palma, Canary Islands, an the genesis of the Caldera de Taburiente. *J. Volcanol. Geotherm. Res.* **1994**, *60*, 243–262. [CrossRef]
187. Guillou, H.; Carracedo, J.C.; y Day, S.J. Dating of the Upper Pleistocene-Holocene volcanic activity of La Palma using the unspiked K—Ar technique. *J. Volcanol. Geotherm. Res.* **1998**, *86*, 137–149. [CrossRef]

188. Carracedo, J.C.; Day, S.J.; Guillou, H.; Gravestock, P. Later stages of volcanic evolution of La Palma, Canary islands: Rift evolution, giant landslides, and the genesis of the Caldera de Taburiente. *Geol. Soc. Am. Bull.* **1999**, *111*, 755–768. [CrossRef]
189. Carracedo, J.C.; Day, S.S.; Guillou, H.; Pérez Torrado, F.J. Giant quaternary landslides in the evolutjon of La Palma and El Hierro, Canary Islands. *J. Volcanol. Geotherm. Res.* **1999**, *94*, 165–190.
190. Guillou, H.; Carracedo, J.C.; Duncan, R.A. K-Ar, ^{40}Ar-^{39}Ar ages and magnetostratigraphy of Brunhes and Matuyama lava sequences from La Palma Island. *J. Volcanol. Geotherm. Res.* **2001**, *106*, 175–194. [CrossRef]
191. Singer, B.S.; Relle, M.K.; Hoffman, K.A.; Battle, A.; Laj, C.; Guillou, H.; Carracedo, J.C. Ar/Ar ages from transitionally magnetized lavas on La Palma, Canary Islands, and the geomagnetic instability timescale. *J. Gephysical Res.* **2002**, *107*, 2307. [CrossRef]
192. Hildenbrand, A.; Gillot, P.-Y.; Soler, V.; Lahitte, P. Evidence for a persistent uplifting of La Palma (Canary Islands), inferred from morphological and radiometric data. *Earth Planet. Sci. Lett.* **2003**, *210*, 277–289. [CrossRef]
193. Quidelleur, X.; Carlut, J.; Soler, V.; Valet, J.P.; Gillot, P.Y. The age and duration of the Matuyama–Brunhes transition from new K–Ar data from La Palma (Canary Islands) and revisited ^{40}Ar/^{39}Ar ages. *Earth Planet. Sci. Lett.* **2003**, *208*, 149–163. [CrossRef]
194. Navarro, J.M.; Coello, J.J. *Mapa Geológico del Parque Nacional de la Caldera de Taburiente*; Ministerio de Agricultura, Pesca y Alimentación: Madrid, Spain, 1993.
195. Fernández, C.; De la Nuez, J.; Casillas, R.; García Navarro, E. Stress fields associated with the growth of a large shield volcano (La Palma, Canary Islands). *Tectonics* **2002**, *21*, 367–384. [CrossRef]
196. Urgeles, R.; Canals, M.; Baraza, J.; Alonso, B. Seismostratigraphy of the western flanks of El Hierro and La Palma (Canary Islands): A record of Canary Islands volcanism. *Mar. Geol.* **1998**, *146*, 225–241. [CrossRef]
197. Krastel, S.; Schmincke, H.; Jacobs, C.L. Formation of submarine canyons on the flanks of the Canary Islands. *Geo-Mar. Lett.* **2001**, *20*, 160–167. [CrossRef]
198. Masson, D.G.; Watts, A.B.; Gee, M.J.R.; Urgeles, R.; Mitchell, N.C.; Le Bas, T.P.; Canals, M. Slope failures on the flanks of the Canary Islands. *Earth-Sci. Rev.* **2002**, *57*, 1–35. [CrossRef]
199. Acosta, J.; Uchupi, E.; Muñoz, A.; Herranz, P.; Palomo, C.; Ballesteros, M.; ZEE Working Group. Geologic evolution of the Canarian Islands of Lanzarote, Fuerteventura, Gran Canaria and La Gomera and comparison of landslides at these island with those at Tenerife, La Palma and El Hierro. *Mar. Geophys. Res.* **2003**, *24*, 1–40. [CrossRef]
200. Colmenero, J.R.; de la Nuez, J.; Casillas, R.; Castillo, C. Caracteres de los conglomerados y brechas epiclásticos de La Palma (Islas Canarias) y su relación con grandes deslizamientos y génesis de la Caldera de Taburiente. *Geotemas* **2008**, *10*, 123–126.
201. Colmenero, J.R.; de la Nuez, J.; Casillas, R.; Castillo, C. Epiclastic deposits associated with large-scale landslides and the formation of erosive calderas in oceanic islands: The example of the La Palma Island (Canary Archipelago). *Geomorphology* **2012**, *177–178*, 108–127. [CrossRef]
202. Hernández-Pacheco, A.; De la Nuez, J. Las extrusiones sálicas del sur de la isla de La Palma. *Estud. Geológicos* **1983**, *39*, 3–30.
203. Day, S.; Carracedo, J.C.; Guillou, H.; Gravestock, P. Recent structural evolution of the Cumbre Vieja Volcano, La Palma, Canary Islands: Volcanic rift zone reconfiguration as a precursor to volcanic flank instability? *J. Volcanol. Geothernal Res.* **1999**, *94*, 135–167. [CrossRef]
204. Hernández-Pacheco, A. La erupción del Tahuya en 1585 y el origen de los Roques de Jedey, La Palma, Canarias. Secretariado de Publicaciones de la Universidad de La Laguna, Tomo Homenaje al prof. *Telesforo Bravo* **1990**, *94*, 425–446.
205. Hernández-Pacheco, A.; Valls, C. The historic eruptions of La Palma Island (Canaries). Arquipelago, Universidade dos Açores. *Série Ciências Da Nat.* **1982**, *3*, 83–94.
206. Carracedo, J.C.; Day, S.; Guillou, H.; Rodríguez Badiola, E. The 1677 eruption of La Palma, Canary Islands. *Estud. Geológicos* **1996**, *52*, 103–114. [CrossRef]
207. Carracedo, J.C.; Troll, R. *The Geology of the Canary Islands*; Elsevier: Amsterdam, The Netherlands, 2016.
208. Black, L.P.; Kamo, S.L.; Allen, C.M.; Aleinikoff, J.A.; Davis, D.W.; Korsch, J.R.; Foudolis, C. TEMORA 1: A new zircon standard for Phanerozoic U–Pb geochronology. *Chem. Geol.* **2003**, *200*, 155–170. [CrossRef]
209. Claoue-Long, J.C.; Compston, W.; Roberts, J.; Fanning, C.M. Two Carboniferous ages: A comparison of SHRIMP zircon dating with conventional zircon ages and ^{40}Ar/^{39}Ar analysis. In *Geochronology Time Scales and Global Stratigraphic Correlation*; Berggren, W.A., Kent, D.V., Aubry, M.P., Hardenbol, J., Eds.; Special Publication No. 4; Society for Sedimentary Geology: Broken Arrow, OK, USA, 1995; Volume 4, pp. 3–21.
210. Williams, I.S.; Claesson, S. Isotopic evidence for the Precambrian provenance and Caledonian metamorphism of high grade paragneisses from the Seve Nappes, Scandinavian Caledonides. II: Ion microprobe zircon U–Th–Pb. *Contrib. Mineral. Petrol.* **1987**, *97*, 205–217. [CrossRef]
211. Dodson, M.H. A linear method for second-degree interpolation in cyclical data collection. *J. Phys. E Sci. Instrum.* **1978**, *11*, 296. [CrossRef]
212. Williams, I.S. U-Th-Pb Geochronology by Ion Microprobe. In *Applications of Microanalytical Techniques to Understanding Mineralizing Processes*; McKibben, M.A., Shanks, W.C., III, Ridley, W.I., Eds.; Reviews in Economic Geology; Mineralogical Society of America: Washington, DC, USA, 1998; Volume 7, pp. 1–35.

213. Williams, I.S.; Hergt, J.M. U-Pb dating of Tasmanian dolerites: A cautionary tale of SHRIMP analysis of high-U zircon. In *Beyond 2000: New Frontiers in Isotope Geoscience*; Woodhead, J.D., Hergt, J.M., Noble, W.P., Eds.; Abstracts and Proceedings; Lorne: New York, NY, USA, 2000; pp. 185–188.
214. Koppers, A.A.P. ArArCALC—Software for Ar-40/Ar-39 age calculations. *Comput. Geosci.* **2002**, *28*, 605–619. [CrossRef]
215. Renne, P.R.; Balco, G.; Ludwig, K.R.; Mundil, R.; Min, K. Response to the comment by W.H. Schwarz et al. on "Joint determination of ^{40}K decay constants and ^{40}Ar*/^{40}K for the Fish Canyon sanidine standard and improved accuracy for ^{40}Ar/^{39}Ar geochronology" by P.R.Renne et al. (2010). *Geochim. Cosmochim. Acta* **2011**, *75*, 5097–5100. [CrossRef]
216. Renne, P.R.; Mundil, R.; Balco, G.; Min, K.W.; Ludwig, K.R. Joint determination of ^{40}K decay constants and ^{40}Ar*/^{40}K for the Fish Canyon sanidine standard and improved accuracy for ^{40}Ar/^{39}Ar geochronology. *Geochim. Cosmochim. Acta* **2010**, *74*, 5349–5367. [CrossRef]
217. De Rosen-Spence, A.F.; Provost, G.; Dimroth, E.; Gochnauer, K.; Owen, V. Archean subaqueous felsic flows, Rouyn-Noranda, Quebec, Canada, and their Quaternary equivalents. *Precamb. Res.* **1980**, *12*, 43–77. [CrossRef]
218. Cas, R.A.F. Submarine volcanism: Eruption styles, products, and relevance to understanding the host-rock succesions to volcanic-hosted massive sulphidedeposits. *Econ. Geol.* **1990**, *87*, 511–541. [CrossRef]
219. Morgan, L.A.; Schultz, K.J. 5. Physical Volcanology of Volcanogenic Massive Sulfide Deposits 2012. In *Scientific Investigations Report 2010–5070–C*; U.S. Department of the Interior and U.S. Geological Survey: Washington, DC, USA, 2012; pp. 63–100.
220. Scutter, C.; Moore, C.L.; Cas, R.A.F. Facies architecture and origin of a submarine rhyolitic lava flow–dome complex, Ponza, Italy. *J. Geophys. Res.* **1998**, *103*, 27551–27566. [CrossRef]
221. Gifkins, C. Textural and Chemical Characteristics of Diagenetic and Hydrothermal Alteration in Glassy Volcanic Rocks: Examples from the Mount Read Volcanics, Tasmania. *Econ. Geol.* **2000**, *96*, 973–1002. [CrossRef]
222. Stewart, A.L.; McPhie, J. Facies architecture and Late Pliocene—Pleistocene evolution of a felsic volcanic island, Milos, Greece. *Bull. Volcanol.* **2006**, *68*, 703–726. [CrossRef]
223. Mulder, T.; Alexander, J. The physical character of subaqueous sedimentary density flow and their deposits. *Sedimentology* **2001**, *48*, 269–299. [CrossRef]
224. Lowe, D.R. Sediment-gravity flows, II: Depositional models with special reference to the deposits of high-density turbidity currents. *J. Sediment. Petrol.* **1982**, *52*, 279–297.
225. Mutti, E.; Tinterri, R.; Remacha, E.; Mavilla, N.; Angella, S.; Fava, L. *An Introduction to the Analysis of Ancient Turbidite Basins from an Outcrop Perspective*; Continuing Education Course Note; American Association of Petroleum Geologists: Tulsa, OK, USA, 1999; Volume 39, pp. 1–96.
226. Le Maitre, R.W. *Igneous Rocks a Classification and Glossary of Terms Recommendations of the International Union of Geological Sciences, Sub-Commission on the Systematics of Igneous Rocks*; Cambridge University Press: Cambridge, UK, 2002; p. 236. [CrossRef]
227. Klügel, A.; Hansteen, T.H.; van den Bogaard, P.; Strauss, H.; Hauff, F. Holocene fluid venting at an extinct Cretaceous seamount, Canary archipelago. *Geology* **2011**, *39*, 855–858. [CrossRef]
228. Metletidis, S.; Di Roberto, A.; Pompilio, M.; Bertagnini, A.; Iribarren, I.; Felpeto, A.; Torres, P.A.; D'Oriano, C. Xenopumices from the 2011– 2012 submarine eruption of El Hierro (Canary Islands, Spain): Constraints on the plumbing system and magma ascent. *Geophys. Res. Lett.* **2012**, *39*, L17302. [CrossRef]
229. Winchester, J.A.; Floyd, P.A. Geochemical discrimination of different magma series and their differentiation products using immobile elements. *Chem. Geol.* **1976**, *20*, 325–343. [CrossRef]
230. López Ruiz, J.; Cebriá, J.M. *Ceoquímica de Los Procesos Magmáticos*; Editorial Rueda: Madrid, Spain, 1990; p. 168.
231. Sun, S.; McDonough, W.F. *Implications for Mantle Composition and Processes Chemical and Isotopic Systematics of Oceanic Basalts: Geological Society*; Special Publications; Geological Society: London, UK, 1989; Volume 42, pp. 313–345.
232. Thompson, G.; Bryan, W.B.; Frey, F.A.; Dickey, J.S.; Davies, H.L. Petrology, geochemistry and original tectonic setting of basalts from the Mozambique Basin and Ridge (DSDP Sites 248, 249 and 250), and from the Southwest Indian Ridge (DSDP Site 251). *Mar. Geol.* **1982**, *48*, 175–195. [CrossRef]
233. Van den Bogaard, P. The origin of the Canary Island Seamount Province—New ages of old seamounts. *Sci. Rep.* **2013**, *3*, 2107. [CrossRef] [PubMed]
234. Fernández-Santín, S. Procesos de propilitización en rocas sálicas del Complejo Basal de la isla de La Gomera. *Com. III Asamb. Nac. Geod. Geof.* **1979**, *3*, 1633–1654.